Title

High Pressure NMR Hardware and Methodologies for the Study of Heterogeneous, Ill-Defined Systems at Low Field

Author

Kerr, Julia DeEtte

Publication Date

2022

Peer reviewed|Thesis/dissertation

High Pressure NMR Hardware and Methodologies for the Study of Heterogeneous, Ill-Defined Systems at Low Field

By

JULIA DEETTE KERR
DISSERTATION

Submitted in partial satisfaction of the requirements for the degree of

Doctor of Philosophy

in

Chemistry

in the

OFFICE OF GRADUATE STUDIES

of the

UNIVERSITY OF CALIFORNIA

DAVIS

Approved:

Matthew P. Augustine, Chair

William H. Casey

Michael McCarthy

Committee in Charge

2022

High-Pressure NMR Hardware and Methodologies for the Study of Heterogeneous, Ill-Defined Systems at Low Field

By

Julia Kerr

Abstract

A high-volume, high-pressure nuclear magnetic resonance (NMR) probe was developed to be amenable to realistic samples and accommodated by a variety of low-field magnetic assemblies. This high volume, pressure probe was made in response to existing high-pressure probes that could not accommodate samples in excess of a couple milliliters. Initial research with industrial samples of petrol and biomass pretreatment showed that current high-pressure NMR assemblies were not amenable to research with heterogeneous industrial samples, due to their high cost and low volume. The high-pressure NMR probe discussed here was assembled from commercially available parts, modifying a pressure reactor to incorporate a high-pressure NMR probe and circuit assembly. This probe was developed and tested using single-sided, portable magnets. Using relaxometry, rather than resolved chemical shifts, due to the lowered frequency range, macroscopic properties of liquids and mixtures could be observed in real time over the course of pressurization.

This work on the high-pressure probe allowed the study of mass-transport mechanisms of salts into a food matrix. Magnetic resonance images (MRI) were taken as apple flesh became pressure-impregnated with salts. These images were used to mathematically model the infusion of molecules into food matrices at high pressure, a feat that had not previously been achieved due to the lack of appropriate high-pressure analytical NMR instrumentation. This information is important in the field of food science where mass transport mechanisms in high-pressure assisted infusion have yet to be fully understood.

In addition to the previously mentioned magnetic assemblies, this pressurization probe was interfaced to an opposing pole-facing magnet, an Aspect Instruments imaging magnet, and a SMIS electromagnet. The high-pressure probe was built for high-volume heterogeneous samples. The probe proved robust enough to perform magnetic resonance (MR) relaxometry on other isotopes like sodium, ^{23}Na.

Acknowledgements

"If I have seen further it is by standing on the shoulders of giants" -Isaac Newton

Thank you first and foremost to my parents and my brother, who have steadfastly been by my side every step of the way during this journey called graduate school. I simply could not have done this without your unwavering support. Mom and Dad, from the time you told me I should consider graduate school until now you have seemed to never tire of listening to my stories, problems, or queries for advice. You have been constants throughout this process and supports I could always rely on, especially when I needed support the most. You helped me keep focused for 6 years to reach this point. There are not enough words to express my gratitude. You are both an inspiration to me. Alex, thank you for everything you have done for me though out graduate school. You were always there open to talking about what was going on and there right when I needed you.

I would be remiss if I did not acknowledge my grandparents. Though they have not been with us for some time, their support of my curiosity, pursuit of science, and academic interest is with me every day. I would like to especially thank my grandfather, Dr. Robert Holland, and grandmother, Dr. Sarah Kerr, for being role models in showing me that a Ph.D. was possible and not something too intimidating to pursue. Dr. Sarah Kerr has been a particular role model for me having both her doctorate and masters, in separate fields, like I now have. I am excited and proud to be our family's next Dr. Kerr.

To Matt, thank you for your constant support and belief in me as a scientist. Your support of all my crazy ideas to join the social media team, TA 75% in my first quarter working for you, take extra classes, and ultimately purse an MBA, all while doing my Ph.D. research, has meant the world to me. It allowed for me to have a unique and fulfilling graduate school experience. Your continued support as I look for

jobs gives me confidence and helps me believe that I truly have learned enough to warrant a doctorate. I didn't know what I wanted in a PI when I came to Davis, but I couldn't have found a better one.

Thank you to my lab mates and mentors. A special thanks needs to go to Dr. Gerardo Ochoa who introduced me to high pressure NMR, taught me to how solder NMR circuits, and generally took me under his wing when I joined Matt's lab. Thank you for your mentorship and teaching. Dr. Michele Martin, thank you for your leadership in the lab, teaching me NMR, and for your patience with me when I needed help troubleshooting. Thank you Dr. Tricia Wong for introducing me to the lab and your mentorship. And last, but my no means least, thank you Dr. Daniel Gruber. You have taught me electronics and upper level physics, critiqued my writing, been my co-Ta, a collaborator, an all-around amazing lab mate, and most importantly a great friend.

Thank you to Professor William Casey and his students Dr. Chris Colla and Dr. Corey Pilgrim for teaching me and training me on high pressure NMR. The foundational information you taught me in my early graduate school years laid the foundation for the work found in this dissertation.

There are many others who deserve thanks in getting me to this point. I cannot name you all but know that I am grateful for all in my life who have supported me and helped me get here.

Table of Contents

List of Figures

Figure 1.14: Selected examples of NMR probes constructed in this work. (a.) Probe to hold an NMR pressure cell in an MRI assembly. The sample was encased in the pressure cell. (b.) High pressure probe made to interface with multiple magnet assemblies. (c.) NMR probe made out of industrial pipe, developed to interface with an MRI magnet assembly.

Figure 1.15: Schematics for two tank circuits used in NMR probes. L denotes the inductors and C_n (n=1,2) denotes capacitors.

Figure 2.1: Schematics and pictures of the HiP-NMR probe. The stainless steel HiP pressure reactor is on the left and the added copper NMR circuit ground shield is on the right in the photograph of the HiP-NMR probe shown in (a). A schematic of the probe showing the plastic coil sleeve is provided in (b). The Berylco – 25 coil, plastic sleeve, and NMR detection circuit in the photograph in (c) are drawn in the schematic (d).

Figure 2.2: Timing diagrams for the NMR pulse sequences. The coupling of the inversion recovery with the CPMG pulse sequence in (a) and the spin echo with the CPMG pulse sequence in (b) respectively provided ^{1}H T_1/T_2^{cpmg} and T_2^{echo}/T_2^{cpmg} correlation data as a function of pressure for this work.

Figure 2.3: HiP-NMR probe with unilateral magnets. The HiP-NMR probe is easy to use. Simple placement on the linear magnet array in (a), or on the cylindrical magnet array in (b) leads to measurable signals.

Figure 2.4: Two dimensional ILT processed ^{1}H relaxation correlation data. These PDMS data sets were obtained using the linear magnet array at 100 MPa pressure. The ILT is used to convert the raw transient signals produced by the pulse sequences in Figs. 2(a) and (b) to the respective T_1/T_2^{cpmg} and T_2^{echo}/T_2^{cpmg} correlations in (a) and (b).

Figure 2.5: Summary of the ^{1}H T_1/T_2^{cpmg} cross peak position in PDMS as a function of pressure and magnet. The squares and circles respectively correspond to measurements obtained from the linear and cylindrical magnet arrays. The gray line is included as a guide to the eye.

Figure 2.6: Summary of the ^{1}H T_2^{echo}/T_2^{cpmg} cross peak position in PDMS as a function of pressure and magnet. The squares and circles respectively correspond to measurements obtained from the linear and cylindrical magnet arrays. The gray lines are included as a guide to the eye.

Figure 3.1: Timing diagram comparing the static 80 MPa pressure in (a), cycled 20 MPa pressure in (b), static 20 MPa pressure in (c), ramped pressure up to 80 MPa in (d) and ambient pressure in (e) pressurization strategies. Each pressurization run typically lasted 4.5 hours while the pressure changes indicated in the diagram, that include a 5 minute equilibration period, lasted roughly 10 minutes.

Figure 3.2: The graphics on the left can be used to understand the real MRI data shown on the right. The top and side views of a cubic apple section are described by the gray solid box on the left in (a) and (b). The white region in these 2D diagrams corresponds to the bulk doped solution outside of the cubic apple section. The 1D slices shown in (c) and (d) were obtained at the location of the white dashed line in (b). the open gray box on the right hand side of (c) and (d) indicates the image region where Equation (3.1) is valid while the solid gray box defines the range $0 < \alpha < 1$ in Equation (3.2).

Figure 3.3: The calculated 1D slices on the left can be used to understand the real MRI data on the right obtained at 80 MPa applied external pressure. The peel is located at –4 mm in all images. The 1D image at the short time, or 40 minutes into the pressure run, in (a) appears to fill in from the side opposite the peel in (b) obtained after 160 minutes at pressure.

Figure 4.1: Timing diagrams for the NMR pulse sequences used in this work. The inversion recovery pulse sequence in (a) and the spin echo pulse sequence in (b) were used to measure ^{23}Na T_1 and T_2^{echo} values as a function of pressure, while (a) and the pulse sequence in (c) were used to measure ^{1}H T_1 and T_2^{cpmg} values. The PGSE sequence in (d) was used to determine D values. Results and Discussion

Figure 4.2: Summary of the ^{23}Na T_1 and T_2^{echo} values for Na2SiO3 as a function of pressure.

Figure 4.3: Summary of the ^{1}H T_1 and T_2^{cpmg} values for Na_2SiO_3 as a function of pressure.

Figure 4.4: Summary of the ^{1}H NMR determined D values as a function of pressure.

List of Abbreviations

1D	One dimensional
2D	Two dimensional
CPMG	Carr-Purcell-Meiboom Gill pulse sequence
D	Diffusion
EMF	Electromotive Force
FID	Free Induction Decay
FTNMR	Fourier Transform Nuclear Magnetic Resonance
FWHM	Full width at half max
^{1}H	hydrogen
HPP	High pressure food processing
MR	Magnetic resonance
MRI	Magnetic resonance imaging
^{23}Na	Sodium
NMR	Nuclear magnetic resonance
PGSE	Pulsed gradient spin echo pulse sequence
Rf	Radio frequency

Chapter 1. NMR Background

1.1 Introduction

Nuclear Magnetic Resonance (NMR) is an analytical technique that uses nuclear spin to elucidate both microscopic and macroscopic properties of chemicals. The central subject of this manuscript is a high volume, high pressure probe that was developed and used with inhomogeneous samples. The new high pressure probe interfaces with low magnetic field, less than 1 Tesla, assemblies, which generally rely on magnetic resonance (MR) relaxation to convey chemical information. MR relaxometry is used to elucidate macroscopic properties and build MR images (MRI). Relaxation parameters can be used to characterize macroscopic chemical properties like rheology, density, viscosity, and molecular tumbling. Physical properties of samples at various pressures were studied using these relaxation parameters. MR images of food matrices under pressure were used to model mass transport of pressurized infusion.

All samples discussed in Chapters 2-4 were pressurized using hydrostatic pressure and studied in situ using MR relaxometry. The values of T_1, T_2, and diffusion (D) were measured. Measurements were taken of samples at ambient pressure and again when pressure increased. The change in values of these parameters are shown to describe macroscopic sample changes.

Macroscopic properties of chemicals and foodstuffs under pressure are studied. The MR probe was developed to monitor changes in samples at pressure. The probe can reach pressures as high as 100 MPa. This pressure is commonly found at the bottom of the ocean floor, a relevant pressure for both oil wells and high pressure food processing (HPP) [1]. HPP is a common technique in the food industry, widely adopted [2], and sometimes referred to as cold pasteurization.

The development and testing of the high pressure NMR probe using a common surfactant, polydimethylsiloxane, is presented in Chapter 2. The methodology was validated with simple techniques.

Proton NMR was performed using the high pressure set up with a single-sided magnet at pressure and ^{1}H NMR relaxation parameters were obtained.

Chapter 3 covers the use of this new hardware in combination with MRI. The high pressure probe was used to image the infusion of bulk water into a food matrix to help understand the mass transport mechanisms for high-pressure assisted infusion [3]. The mass transport involved in high pressure-assisted infusion is of interest to food scientists [4]. The main roadblock to accomplish this work in situ is, again, the lack of an analytical technique that can be used to investigate during pressurization. MR imaging was used to study the infusion of salts into a model fruit flesh matrix. The salts were used as an MRI contrast reagent and as a small molecule model. The results and methodologies for MR images obtained using the high pressure hardware at the heart of this thesis is discussed. Moreover, a relationship between experimental data and mass transport, embodied by the infusion coefficient D_{inf}, is introduced to and used to obtain mass transport details.

Chapter 4 demonstrates the robustness of the probe and describes the use of this new high pressure probe technique with a different nucleus. Sodium (^{23}Na) NMR spectral relaxometry data were obtained for sodium silicate as a function of pressure. This chapter also describes the use of the new hardware to map out macroscopic properties of the sodium silicate adhesive under pressure. Again, experiments convey the superb robustness of this high pressure probe.

1.2 What is Spin?

Spin is an intrinsic property of a particle [5]. Like charge or mass, spin just is. Electrons, protons, neutrons, atoms, photons, nuclei, all have spin. All of these particles have fundamental masses, charges, and spin values. These spin values describe the inherent angular momentum of a particle. Even though spin describes the possession of angular momentum, it does not mean that the particle in question is actually spinning. Spin, is unfortunately, somewhat of a quantum-mechanical misnomer.

Spin in general describes the angular momentum, but since spin is an intrinsic property, it refers specifically to the intrinsic angular momentum - the angular momentum that is always possessed by the particle of interest. Often when angular momentum is pondered, it is in reference to some external standard. The angular momentum of an electron about a nucleus or the moon about the earth are examples. In those cases, the angular momentum would quantum mechanically be referred to as orbital angular momentum rather than spin. Quantum mechanical spin does not describe the angular momentum of a particle around an external object, as it is a fundamental and inherent property. Protons, neutrons, and electrons always have a value of spin ½, photons always have a value of spin 1, etc.

NMR is concerned with the intrinsic non-orbital spin, commonly referred as just 'spin'. Spin is assigned quantum mechanically. The electron spin quantum number refers to electrons and the nuclear spin quantum number refers to nuclei. The spin magnetic quantum number can be used to describe a spin when it is being acted on by an external magnetic field [6]. It denotes how the spin angular momentum is to be projected onto the Z-axis in the presence of a magnetic field. The z-axis runs parallel to the magnetic field, B. This means the component of the spin vector that lies in the direction of the B field. When the components of the spin are described, a vector model emerges. A depiction of (+) and (–) spins in a vector model can be seen in Figure 1.1. The projection of the spin vector onto the z axis is also illustrated.

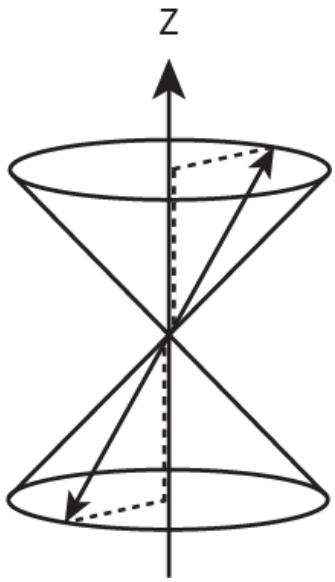

Figure 1.1: Vector model of two spins and their projections onto the Z-axis denoted by dotted lines. The spin projection of one spin aligns with the Z-axis and is considered spin up while the second spin projection does not align and is considered spin down.

The Z direction denotes the axis that is aligned with the B field. The spins are represented by arrows. There are two spins represented, one aligned, spin (+) and one anti-aligned, spin (-) [7]. The spins depicted on the two conical surfaces in Figure 1.1 because they do not directly align, or anti align with a magnetic field. The spins precess about the z-axis. This spin precession is known as Larmor precession [8]. The frequency at which the spins precess about is called the Larmor frequency. It is because of this precession that the spins are represented on conical surfaces about the z axis. The lack of direct alignment with the field is why the spin magnetic quantum number described by the projection of a spin onto the z axis. The projection of the spin onto the z axis is represented by dotted lines in Figure 1.1 is what determines if a spin is up or down is the direction of the Z-axis spin. If the projection of the spin on the z-axis aligns, the then spin is spin up. If the projection anti-aligns, the spin is considered spin down. The value of the spin stays consistent just the projection of the spin can change.

The quantization of spin values was experimentally proven by the now famous Stern-Gerlach experiment. The Stern-Gerlach experiment involved passing a beam of silver atoms through an

inhomogeneous magnetic field [6]. The result was the silver beam ended up split into two bands. This showed that spin indeed was quantized, and in this case, the value is $\hbar/2$.

Nuclei often contain multiple particles that have spin 1/2. The nuclear spin quantum number, I, is obtained from a combination of spins in the nucleus [9]. Spin-up and spin-down fermions pair up to cancel each other out. The Pauli principle dictates that neutrons and protons only pair up with themselves. So, neutrons pair with neutrons and protons pair with protons. he fact that paired up fermions cancel out leaves only unpaired protons and neutrons to determine the overall nuclear spin value. Unpaired fermions of two types, protons and neutrons, allows for integer as well as half integer nuclear spin quantum numbers.

A nucleus with spin greater than zero is considered NMR active [8]. When a nucleus has spin, there is inherent angular momentum. This angular momentum of a positively charged nucleus in space gives rise to a nuclear magnetic moment [9]. A nucleus that has angular momentum and a charge, creates its own magnetic dipole, will thus interact with external magnetic fields. The interactions of a nuclear magnetic moment and an external magnetic field are the underpinnings of NMR. If a nucleus has a net spin of zero, it has no overall angular momentum and the charged nucleus does not create a nuclear magnetic dipole in space. When this happens, the nucleus is considered NMR inactive - it cannot be probed or characterized by NMR.

NMR active atoms have nuclei that possess a nuclear magnetic moment. When a collection of nuclei with dipole moments are placed into a magnetic field, the individual nuclear spins align in one of two quantum states: spin up (+), aligned with the magnetic field, or spin down (-), aligned against the magnetic field. In the absence of a magnetic field, there is no common projection direction, the spins point in random directions and thus the net magnetic dipole is zero. Figure 1.2 shows a simple vector model of

nuclear spins at thermal equilibrium with and without a magnetic field. Spins are not aligned outside of a magnetic field and aligned when in the presence of a magnetic field.

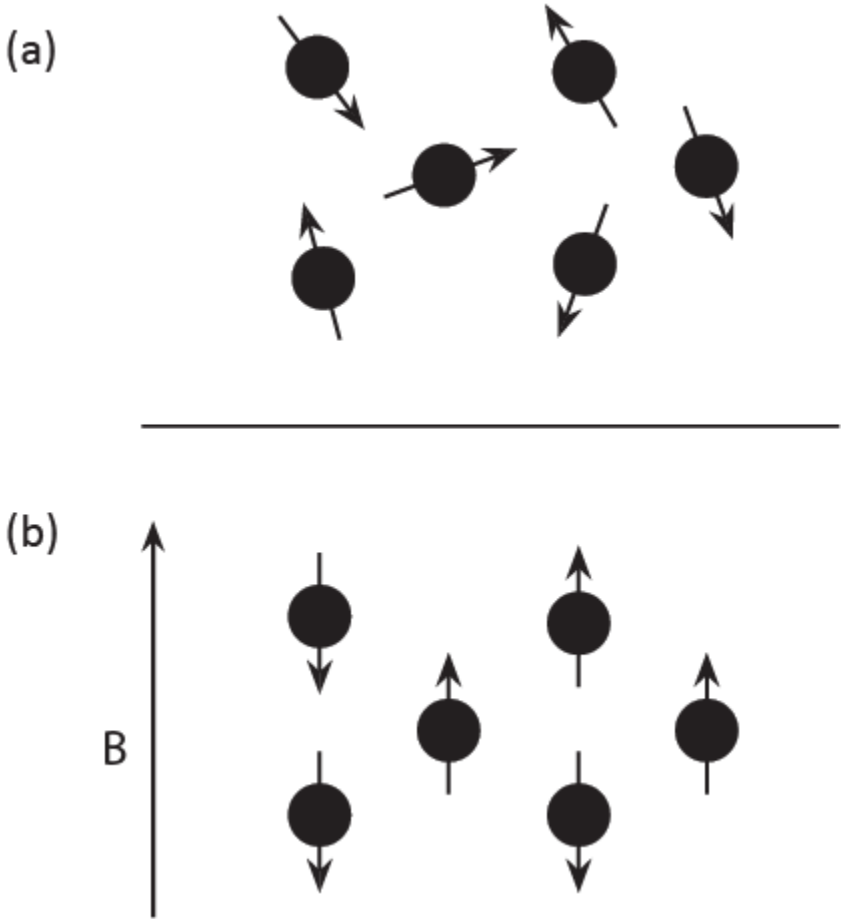

Figure 1.2: (a.) Nuclear spins in zero magnetic field. (b.) Nuclear spins aligned with and against an applied magnetic field.

As discussed before, the overall spin of a nucleus is determined by the net value of the unpaired spins comprising the nucleus. It is the unpaired spins that determine the spin state of the nucleus. Spins can be 'flipped' from one spin state to the other when given the right amount of energy. The energy needed to flip spin states is equal to the energy difference between the spin states in an applied magnetic field. The energy required to flip spin states is associated with the Larmor frequency of the spin. The Larmor frequency of a spin is defines as

$$\omega = \gamma B \tag{1.1}$$

where ω is the Larmor frequency, γ is the gyromagnetic ratio, and B is the magnetic field. The difference in energy between the spin states, and Larmor precession frequency of a nucleus, is not fixed. It is dependent on both the nucleus and the strength of the magnetic field. The stronger the magnetic field, the greater the difference in spin states energy. This relationship is visually depicted by a Zeeman splitting diagram in Figure 1.3.

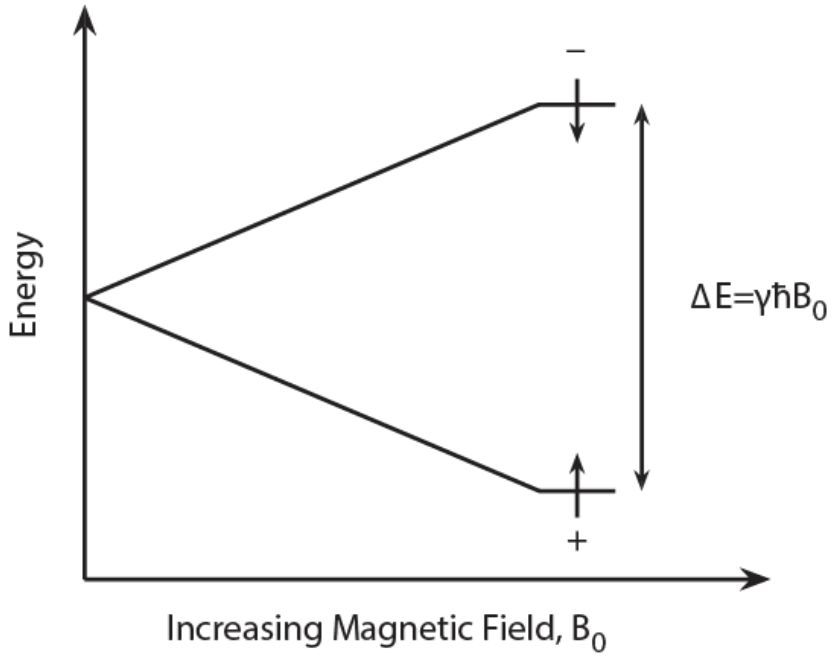

Figure 1.3: A Zeeman splitting diagram where ħ is the reduced Planck constant and γ is the gyromagnetic ratio.

The Zeeman splitting diagram shows the quantized energy levels for spin up and spin down and their associated splitting [7]. As the strength of the external magnetic field, B, increases the difference in the spin (+) and spin (–) energy levels increase as prescribed by the Zeeman energy

$$\Delta E = \gamma \hbar B \tag{1.2}$$

where ΔE is the difference between the energy levels and $\hbar$ is the reduced Planck constant. The spin up (+) state is shown lower on the energy axis because the aligned spins have lower energy than the anti-aligned spins. The difference in energy of the spin states dictates the amount of energy needed to flip a spin from one spin state to the next. For NMR, this energy is given in the form of radio waves. Radio waves, at the correct frequency, deliver the appropriate energy needed to flip a spin. A nuclear spin in the presence of a low B field would need a lower radio frequency (rf) to flip a spin than if the B field were higher. Rf pulses are nucleus selective because each nucleus has defined energy splitting at a specific magnetic field strength as prescribed by the different nucleus specific γ values. Nuclear spins can be selectively flipped by rf based on the B field strength.

Radio waves are be used to flip spins, as spins are flipped the overall magnetization vector is perturbed from its original alignment [10]. When the overall magnetization vector in perturbed from its alignment with a B field, it eventually realigns itself with the field. This realignment process is called spin relaxation. This spin relaxation is at the center of MR relaxometry.

1.3 Insensitivity of NMR

The magnetization of a sample is the magnitude of net nuclear magnetic moment of a sample [6]. The net magnetic moment is also referred to as bulk magnetization. The magnetization of a sample is mathematically described by

$$m_Z = n_+ - n_- \tag{1.3}$$

where m_Z is the bulk or overall magnetization of a sample. The Z subscript denotes the magnetization along the z axis or the axis parallel to the magnetic field. The n_+ and n_- variables are the number of nuclear spins in the sample in either the up (+) or down (-) spin state [11]. The ratio of spin up and spin down populations at thermal equilibrium is described by Boltzmann statistics [11, 12].

$$\frac{n_-}{n_+} = e^{\frac{-\Delta E}{kT}} = e^{\frac{-\hbar\gamma B}{kT}} \quad (1.4)$$

where k is the Boltzmann factor, and T is the temperature, and the Zeeman energy $\Delta E=\gamma\hbar B$ is used. Generally, $kT >> \gamma\hbar B$ and the ratio in equation (1.4) is usually very close to 1 meaning that the difference in spin-state populations is very small. The difference in spin-state populations could theoretically be as low as one spin. It is the fact that the size of the NMR response relies on the difference of one spin or a small amount of spins, in the presence of millions, that causes the technique to be insensitive.

The amount of sample required to get an NMR signal is thousands of times higher than other spectroscopies and analytical methods. Other methods may only need samples on the order of nanoliters, like mass spec, where NMR typically needs samples to be on the order of milliliters to achieve enough signal to obtain relevant chemical information.

Based on (1.4), an increase in energy difference between the spin-up and spin-down quantum states of the particles can change the ratio of spin states and thus overpopulate one spin state versus the other. This phenomenon is why characterization of compounds is done on high magnetic field NMR instrumentation. The higher the field of the magnet, the larger the difference in energy, and the larger the difference in spin state population. When one spin state is overpopulated, there is stronger signal obtained from the same amount of sample. Thus, there is more sensitivity when there is a larger difference in spin state populations and a greater signal intensity per volume of sample. There is more sensitivity because the population difference between spin states is larger. Thus, a higher resolution between chemical shifts in FTNMR, which is usually referred to as NMR spectroscopy.

1.4 MR Relaxometry

MR relaxometry is a subset of magnetic resonance that deals with the measurement of spin relaxation. There are two main spin relaxation parameters, longitudinal spin relaxation, or T_1, and transverse relaxation, or T_2 [13]. These describe the relaxation of nuclear spins after bulk magnetization of a sample is perturbed [7]. In the case of NMR, bulk magnetization is perturbed by energy in the form of radio waves.

The parameters T_1 and T_2 describe the relaxation of spins after they are probed by a rf pulse. T_1 describes the relaxation of the bulk magnetization back to alignment with the B field. T_2 describes the loss of spin coherence in the x-y plane.

Self-diffusion coefficients and molecular tumbling correlation times can be obtained using MR relaxation techniques [14]. Diffusion measures the distance a molecule travels over a given amount of time. The correlation time, or τ_c, is the amount of time it takes for a molecule to rotates through one radian as it tumbles [10].

1.4.1 Bloch equations and classical treatment of T_1 and T_2

MR relaxation parameters T_1 and T_2 can be classically described using the Bloch equations. The Bloch equations look at the bulk magnetization, or total magnetic moment of, a sample [7, 15]. In this case the magnetization is defined by

$$\mathrm{M} = \Sigma_{j=0}\, \mu_j = \frac{(n_+ - n_-)\gamma\hbar}{2} \tag{1.5}$$

where M is the total sample magnetization and the μ_j are the magnetic moments of the individual spins. Bulk magnetization can also be described in terms of spin angular momentum as

$$\mathrm{M} = \frac{\gamma\hbar P}{2} = \frac{\gamma\hbar}{2}\left(\frac{1 - \mathrm{e}^{\frac{-\gamma\hbar B}{\mathrm{kT}}}}{1 + \mathrm{e}^{\frac{-\gamma\hbar B}{\mathrm{kT}}}}\right) \tag{1.6}$$

Where P is spin polarization written in terms of the Boltzmann factor in equation (1.4). The gyromagnetic ratio, γ, is the characteristic parameter of a nucleus that relates the nuclear magnetic moment to the nuclear angular momentum. The definition of the gyromagnetic ratio is obtained by rearranging

$$\gamma = \frac{2M}{\hbar P} \tag{1.7}$$

The effect of an applied magnetic field, B_1, on a magnetized sample is described by the Bloch equations. The Bloch equations arise from looking at the torque created by the interaction between the overall magnetization of a sample and the magnetic field. The interaction can be represented by a cross product

$$\frac{d}{dt}M = -\gamma B_1 \times \mathrm{M} \tag{1.8}$$

where M is the overall magnetization of the sample and B_1 is the magnetic field. Both M and B_1 are vectors with x, y, and z components since they are describing the components of the overall magnetic field and magnetization of a sample. The two 3 component vectors for magnetization and magnetic field when crossed with one another give a 3 component vector for the overall magnetization in the presence of a magnetic field. This vector still describes the magnetization for each x, y and z component. The separate components of each vector describe the magnetization in the x, y, or z direction. In this way, there is an equation for the magnetization in each Cartesian direction and the equations can be modified to include the effects of relaxation resulting in the Bloch equations coming out as

$$\frac{d}{dt}\mathrm{M_z} = -(\gamma B_1 \times \mathrm{M})_z - \frac{(\mathrm{M_z} - \mathrm{M_0})}{\mathrm{T_1}} \tag{1.9}$$

$$\frac{d}{dt}\mathrm{M}_x = -(\gamma B_1 \times \mathrm{M})_\mathrm{x} - \frac{\mathrm{M_x}}{\mathrm{T_2}} \tag{1.10}$$

$$\frac{d}{dt}\mathrm{M}_y = -(\gamma B_1 \times \mathrm{M})_y - \frac{\mathrm{M}_y}{\mathrm{T_2}} \tag{1.11}$$

In the rotating frame, where the transverse magnetization rotates at the Larmor frequency, these equations reduce to

$$\frac{d}{dt}\mathrm{M_z} = -\frac{1}{T_1}(M_z - M_0) \tag{1.12}$$

$$\frac{d}{dt}\mathrm{M_{x'}} = -\frac{1}{T_2}M_{x'} \tag{1.13}$$

$$\frac{d}{dt}\mathrm{M_{y'}} = -\frac{1}{T_2}M_{y'} \tag{1.14}$$

ordinary differential equations with solutions

$$M_z(t) - M_0 \propto e^{\frac{-t}{T_1}} \tag{1.15}$$

$$M_{xy'}(t) \propto e^{\frac{-t}{T_2}} \tag{1.16}$$

These solutions to the Bloch equations are the exponential relations that describe spin relaxation. They describe both relaxation back to thermal equilibrium, for T_1, and loss of spin coherence, for T_2. The characteristic time constants T_1 and T_2 are calculated using the relations in equations (1.15) and (1.16). T_1 and T_2 are obtained experimentally by fitting sample data to exponentials derived from these solutions.

1.4.2 Longitudinal relaxation time T_1

The parameter T_1 is the longitudinal relaxation time, also known as spin-lattice relaxation. It describes the time that it takes for sample magnetization to develop or align with the B field [9]. Spin-lattice relaxation is the process of spins relaxing back to thermal equilibrium. The T_1 parameter is not technically the time it takes for the spins to relax rather it is the time constant for the exponential

magnetization recovery. T_1 describes the exponential relaxation of sample magnetization. Spins can be induced to relax to thermal equilibrium by a variety of mechanisms [16]. The main contribution for T_1 relaxation are fluctuations in the magnetic field perpendicular to the Z-axis. Tumbling of sample molecules induce dipoles that cause fluctuations in the B field. Fluctuating magnetic fields near Larmor frequencies of spins cause the spins to flip and the overall magnetization of the sample to relax back to equilibrium.

The T_1 value is commonly measured using the inversion recovery [17] or saturation recovery [18] pulse sequences. Inversion recovery inverts the spin populations and detects bulk magnetization at different time points during relaxation [17]. The data collected from the time points builds the exponential curve used for extrapolating T_1. Saturation recovery destroys Z-axis magnetization through a train of rf pulses. Then data points are taken at various delays. The size of the sample magnetization is tracked, and the time points are often logarithmically spaced. As magnetization recovers in an exponential fashion, the T_1 value can be obtained through data fitting. The same exponential fitting equation is used for both inversion and saturation recovery. The timing diagrams for inversion recovery and a saturation recovery are provided in Figure 1.4.

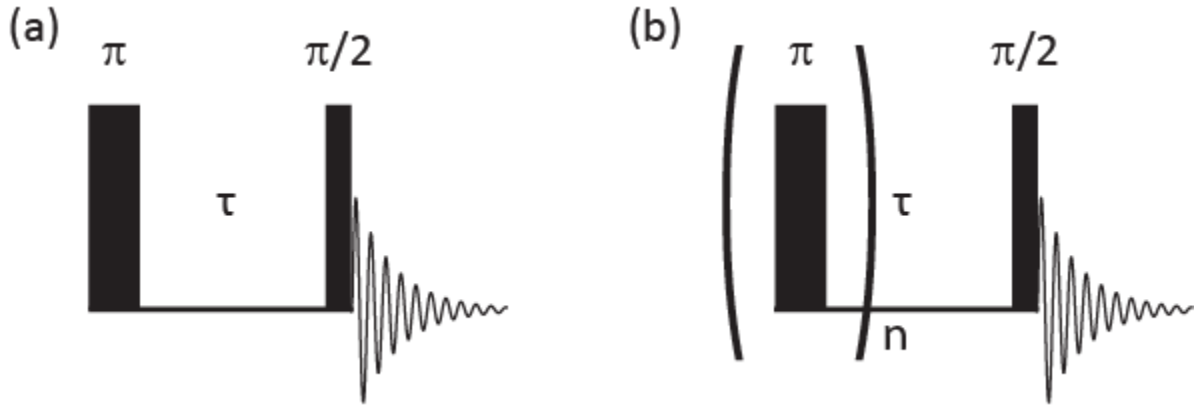

Figure 1.4: Pulse sequence timing diagrams for the (a.) inversion recovery and the (b.) saturation recovery.

The π and π/2 rf pulses are applied to the nucleus of interest. The Θ = π and π/2 communicates the rf tip angle or the extent of rotation about ω_1 at time t of the rf pulse: $\Theta = \omega_1 t$. A π pulse tips the sample magnetization π radians, or 180 degrees. A π/2 pulse tips the magnetization π/2 radians, or 90 degrees.

An inversion recovery pulse sequence involves applying a π pulse followed by a π/2 pulse after some time, τ. Then the detector is opened. The pulses are repeated at numerous time steps of τ until a change in the magnetization vector is no longer detected. When the π/2 pulse is in the +y direction, at the first time point, the detector will 'see' the magnetization vector in the -x direction. Eventually the magnetization will evolve to be in the +x direction when the detector is opened. This pulse sequence is a 2D experiment. This sequence is repeated a set number of times. The time between the π and π/2 pulse, τ, is increased step wise. Free induction decays (FIDs) are obtained for each new time step. This procedure is continued until the FID detected is unchanged by the increase in τ time. The data from the beginning of each FID is used for the exponential fit. The time axis for the exponential fit is the τ value at each step.

Saturation recovery, unlike inversion recovery, does not invert the bulk magnetization. Instead, it destroys the magnetization vector through a series of rf pulses. After the magnetization vector is destroyed, a waiting time is applied, and a π/2 pulse is given. The time between the train of π pulses and the π/2 pulse is denoted by τ. τ is lengthened until the FIDs evolve into full signal, as would be the result of just the π/2 pulse.

Examples of exponential fits created from inversion recovery and saturation recovery experiments can be seen below.

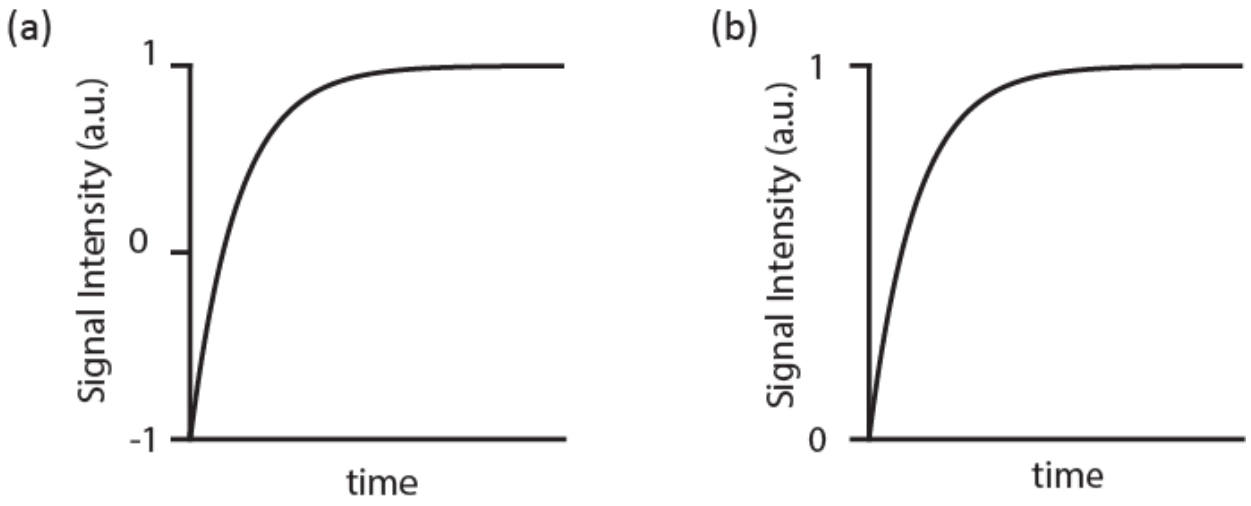

Figure 1.5: Representative exponentials resulting from the (a.) inversion recovery and (b.) saturation recovery pulse sequences to elucidate T_1 values.

Figure 1.5(a) depicts inversion recovery. The exponential starts at the -1 value and goes to 1 on the y axis. This conveys that the magnetization vector is detected in the -x direction for the first time step and in the +x direction for the final time step. The vector is not considered to have changed magnitude which is why the magnitude of both values can be normalized to 1. Figure 1.5 (b) represents a saturation recovery exponential fit. For saturation recovery, the y axis starts at 0 since the magnetization vector is destroyed and recovers with time to the Boltzmann equilibrium value.

1.4.3 Spin-spin relaxation time T_2

The parameter T_2 is known as the spin-spin relaxation time. This relaxation parameter describes how long it takes the spins, or spin packet, to lose coherence in the x-y plane [6]. When the spins are tipped into the x-y plane, they are initially clumped together. As time evolves, the individual spins fan out in a random non-refocusable fashion. This decoherence happens because the individual spins precess at slightly different frequencies [16]. The individual precession frequencies cause the narrow spin packet to decohere and broaden. A graphical representation of the effect is shown here (Figure 1.6).

The parameter T_2 represents the time it takes for the magnetization perpendicular to the B field to dissipate. The dissipation of magnetization is due to the loss of spin packet coherence. T_2 relaxation is driven by some of the similar mechanisms that drive T_1 relaxation, in addition to other ones [16]. The additional mechanisms are one of the reasons that $T_1 \geq T_2$ at all times. There are more relaxation mechanisms for T_2 than T_1. When the bulk magnetization is rotated by a rf pulse into the x-y plane, the magnetization vector in the x-y plane shrinks over time. This magnetization shrinks because the individual spins fan out through spin presession and coherence loss. A simple diagram of this can be seen in Figure 1.6.

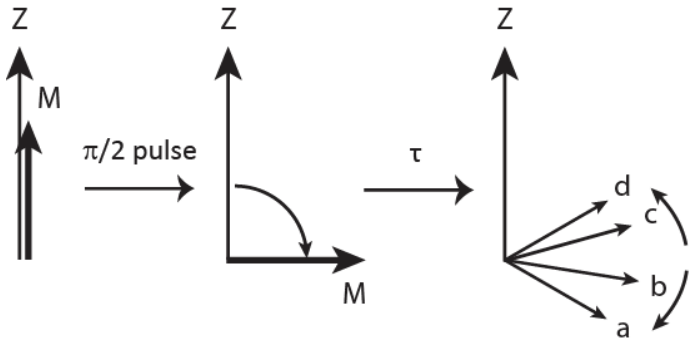

Figure 1.6: A depiction bulk magnetization being rotated into the x-y plane and coherence loss as spins fan out through spin precession.

The parameter T_2 is measured commonly using two-dimensional (2D) spin echo or a one-dimensional (1D) Carr-Purcell-Meiboom-Gill (CPMG) pulse sequence [19, 20]. For the 2D echo experiments, the τ time is varied similar to the pulse sequences for T_1. The pulse sequences timing diagrams for a CPMG and spin echo can be seen in Figure 1.7.

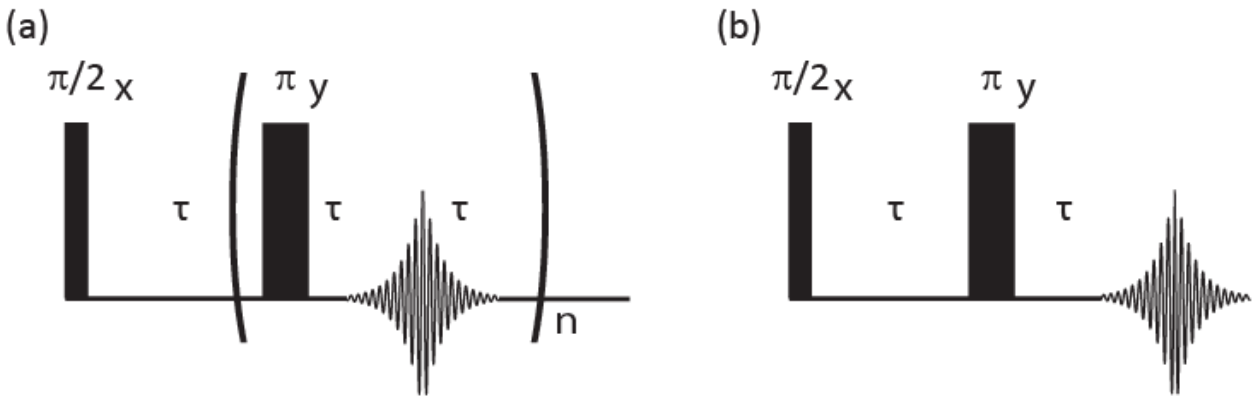

Figure 1.7: Timing diagrams for (a.) CPMG pulse sequence and (b.) spin echo pulse sequence.

A CPMG experiment is essentially the same as a spin echo experiment. In a 2D spin echo experiment the τ time is varied similar to an inversion recovery experiment. CPMG experiments are 1D experiments that induce train of spin echoes. The train of echoes is induced by a train of π pulses. The detector is opened after each π pulse to detect the spin echo signal. The envelope of the train of echoes is in the form of an exponential decay and the envelope represents the shrinkage of the magnetization in the x-y plane and is used to calculate a T_2 value.

A diagram of the vector model for spins during a single spin echo pulse sequence can be seen in Figure 1.8 [19].

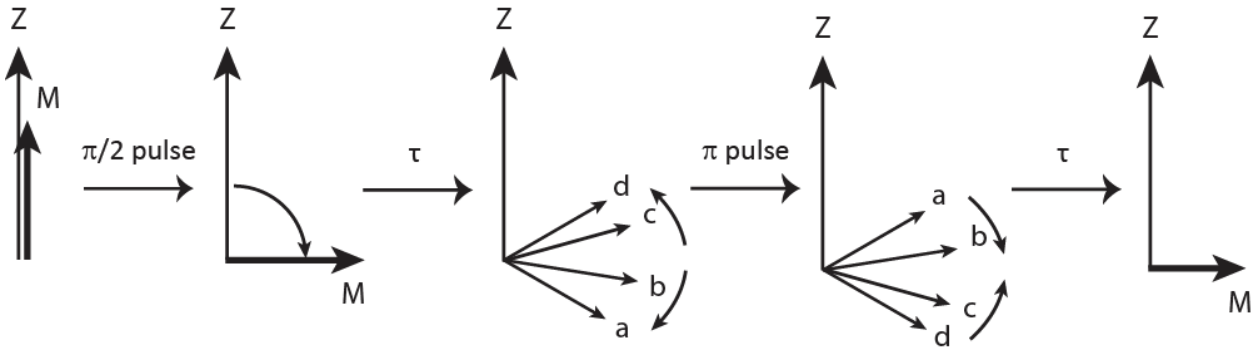

Figure 1.8: Vector model of spins during a single spin echo.

Figure 1.8 depicts spins during a single spin echo. The timing diagram for the spin echo pulse sequence is provided in Figure 1.7(b). The CPMG experiment, with timing diagram shown in Figure 1.7(a), has a similar vector model for spins. The difference is that a CPMG is a train of spin echoes, not a single spin echo. Here the CPMG vector model involves repeating the final three steps n times until the magnetization in the x-y plane is undetectable. In both the 2D spin echo and the CPMG experiments the signal decays exponentially as shown in Figure 1.9. A 2D spin echo experiment would take the data point at the high point of each echo for each τ choice. A fit of the data to an exponential decay yields T_2. With CPMGs, the envelope of the detected spin echoes can be fit to obtain T_2 values.

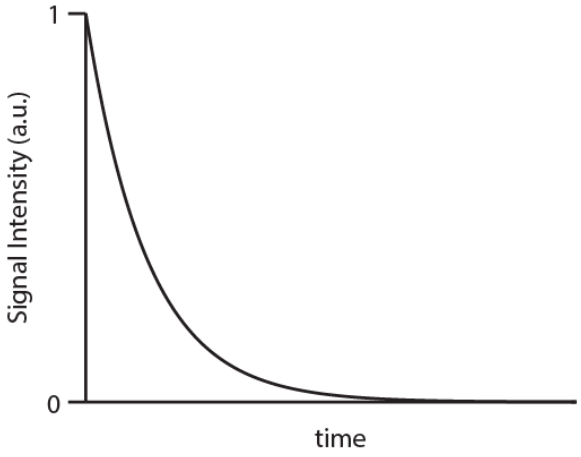

Figure 1.9: Exponential decay that characterizes spin-spin relaxation and is used to obtain T_2.

1.4.4 Diffusion

Diffusion describes the distance a molecule or atom travels per unit time. The common units for diffusion are centimeters squared or meters squared per second. Self-diffusion coefficients describing random translational motion can also be measured with relaxometry. Self-diffusion coefficients are obtained through the use of a pulsed-gradient spin-echo (PGSE) pulse sequence [21]. Diffusion coefficients can be used to calculate further macroscopic properties of a sample—like molecular tumbling and viscosity. Viscosity can be calculated from the diffusion coefficient using the Stokes-Einstein equation [13].

$$\mathrm{D} = \frac{kT}{6\pi\eta\mathrm{r}} \tag{1.17}$$

where D is the self-diffusion coefficient of the molecule of interest, r is the diameter of the particle sphere, and η is the dynamic viscosity. Equation (1.17) is only appropriate during Laminar flow at a low Reynolds number.

Diffusion coefficients mentioned in this dissertation were obtained using the PGSE pulse sequence with timing diagram shown in Figure 1.10 [14]. The PGSE experiment must be done on gradient capable magnet assembly like those common to MR imaging spectrometers.

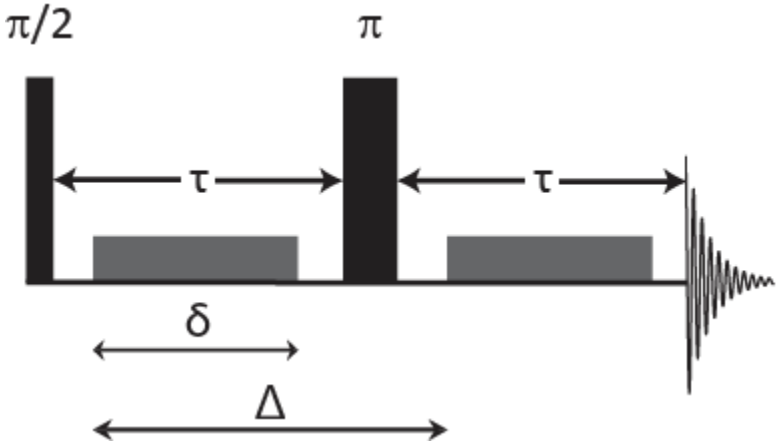

Figure 1.10: A timing diagram for the pulse-gradient spin-echo pulse sequence.

The light grey box in the timing diagram represents the gradient pulse in the sequence and τ is the time between pulse sequences, δ is the gradient pulse length, Δ is the time between the gradient pulses. In the PGSE sequence, the length of time denoted by the variables has a set relation that follows, τ>Δ>δ. The π/2 pulse puts the magnetization in the x-y plane. The gradient pulse spatially dephases the spins in the x-y plane, an effect that is reversed by applying a spin echo (a π rf pulse) followed by a second gradient pulse application. In the absence of random molecular diffusion, the echo recovers to nearly full signal intensity, less the attenuation due to T_2 relaxation. With molecular motion, the spin echo attenuates for

non-zero gradient values. Thus, the 2D diffusion experiment involves tracking the spin echo height as a function of applied gradient strength. This signal decay is used to obtain D values with data fitting.

1.4.5 Correlation time

Correlation time is the time it takes a molecule or nucleus to rotate through one radian. Correlation time associated with rotation is most commonly of interest in NMR. Rotational correlation time is denoted by the variable τ_c [10, 16]. This time quantifies molecular tumbling. When molecular tumbling is high, the correlation time is short. When molecular tumbling is slow, the correlation time is long. Nuclei create nuclear magnetic dipole moments. In the presence of an external magnetic field, B, the dipole moments interact with the B field to create local magnetic fields. These local field environments are what an individual spin experiences in addition to the static B field. The magnetic field experienced by a spin, denoted as B_{eff}, is sum of the applied B field and these local magnetic fluctuations.

Molecular tumbling, as mentioned above, is related to velocity and diffusion. The τ_c and η values are mathematically related as [10]

$$\tau_c = \frac{4\pi\eta a^3}{3kT} \tag{1.18}$$

for a sphere of radius a in a low Reynolds number Newtonian liquid. The similarity in the equations for τ_c and D in equations (1.17) and (1.18) suggest that they can be related as [10]

$$9\tau_c = \frac{2a^2}{D} = \tau_t \tag{1.19}$$

where τ_t is translational correlation time.

The correlation time directly modifies T_1 and T_2 values as the τ_c describes molecular tumbling. Molecular tumbling creates incoherent field fluctuations that manifest in changes to T_1 and T_2 values. The longer a spin experiences incoherent field fluctuations the greater, or more rapid, the relaxation. Local

field environments arise from these fluctuations and allow for auxiliary relaxation pathways to randomize spins back to thermal equilibrium. This increases the rate of spin relaxation. Typically, this means that when there is slow molecular motion, there are more relaxation pathways that lead to shorter T_1 and T_2 values.

When there is a short correlation time, there is rapid molecular tumbling that averages out local magnetic environments providing longer T_1 and T_2 values. The connection between correlation time and relaxation time values, T_n (n=1,2), is illustrated by [11, 21]

$$\frac{1}{T_n} \propto \frac{\langle \omega^2 \rangle \tau_c}{1 + \omega_0^2 \tau_c^2} \tag{1.20}$$

where ω_0 is the Larmor frequency and $\langle \omega^2 \rangle$ is the mean square of the local field fluctuations at a particular frequency, ω. This particular form for the relaxation time in terms of a single Lorentzian-shaped spectral density is overly simplified. In reality, depending on the relaxation mechanism [7], the $\frac{1}{T_n}(n = 1,2)$ values involve a sum of spectral density functions. In all cases, nuclear spin relaxation rates always involve a sum of functions like the one in equation (1.20). Furthermore, in all cases in the extreme narrowing limit where $\omega_0 \tau_c \ll 1$ and in the opposite limit when $\omega_0 \tau_c \gg 1$,

$$T_n \sim \frac{1}{\langle \omega^2 \rangle \tau_c}. \tag{1.21}$$

As mentioned above, the true mathematical forms for T_1 and T_2 involve differently weighted linear combinations of spectral density functions [7]. For fast motion in the extreme narrowing limit, $T_1 \approx T_2$ while for slow motion, $T_1 \gg T_2$. It is the details of the motion captured by the τ_c value that determines this crossover to and from the extreme narrowing limit.

1.5 Other uses for Relaxometry

Relaxometry is a powerful tool as NMR relaxation times can elucidate molecular tumbling, viscosity, and other macroscopic sample properties. Relaxometry is a superb, noninvasive, nondestructive sample comparison tool. MR Relaxometry is a useful NMR tool in instances when high-resolution chemical-shift NMR is not possible, for example in low fields or in awkward geometries. Changes in properties of samples can be probed noninvasively with the use of relaxometry. Relaxometry has been used to detect spoilage in tomato paste [22] and rheological properties of detergent during agitation, amongst other things [23]. In this dissertation relaxometry is used to elucidate the changes in properties of substances under pressure as well as create MR image (MRI) of food stuffs during pressurizations. The food-imaging method in later chapters take advantage of the contrast offered by MR relaxometry to study the penetration of short relaxation time liquids into a long relaxation time medium.

1.5.1 Relaxometry in MRI

The T_1, T_2, and D values are all parameters that can be used to generate contrast in MR images [24]. MR images require magnetic gradients to measure these parameters at discrete spatial points in a sample [25]. There are many techniques and methods for spatial sampling [21]. A common example is k space sampling. Relaxometry parameters are either obtained from desired spatial locations or used to provide image contrast. Numerous sequential MR relaxation experiments are used to construct these images. Once obtained, parameter magnitudes are compared and changed into a color weighting for graphical representation. The image is created based on the experimental spatial-sampling routine. This image construction creates a pixel-by-pixel map of relaxation parameters intensities. Colors and grey scale do not reflect any relaxometry information gathered except for relative magnitude.

Switchable magnet field gradients are necessarily for MRI. Gradients shim, or change, the B field with respect to distance. Generally, shimming gradients are used to make a B field more homogeneous.

In the case of MRI, gradients are used to slightly vary the applied magnetic field over space [21]. This changes the sampling location. This shimming allows for the relaxation parameters to be obtained for specific spatial location.

Generally, in a magnet there is a sweet spot where the B field is most homogeneous. When this is the case, the goal is to have the sample in the homogeneous part of the field and then obtain relaxometry parameters from the sweet spot of the magnetic field. In the case of MRI, gradients shim the field to change the location of the sweet spot. This way relaxometry parameters can be obtained from a variety of spatial locations and still be obtained under homogeneous B field conditions. Not all magnets have gradients or MRI capabilities. MRI magnets are a specific subset of NMR magnet assemblies.

1.5.2 Relaxometry in FTNMR

Fourier Transform NMR (FTNMR) is commonly referred to as NMR spectroscopy. FTNMR is generally performed with high field magnets. FTNMR is usually performed at high field because it allows for higher resolution. More highly resolved spectra provide more chemical structure information. FTNMR spectra are displayed in the frequency rather than time domain and the spectrum is typically a set of Lorentzian shaped peaks [8]. Low-field NMR does not have the magnetic field strength and homogeneity to be able to resolve peaks. This lack of resolution makes it difficult to relate broad and featureless FT spectra to chemical structure.

FTNMR can give information on nuclear coupling and chemical structure. Information about nuclear coupling and chemical structure is unattainable using pure relaxometry. There is still a relationship between the relaxometry parameters and FTNMR spectra [10]. T_1 and T_2 relaxometry parameters govern the shape of the Lorentzian peaks seen in FTNMR. T_1 is correlated to the relative heights of the peaks within a spectrum. While T_2 is inversely related to the full width at half max (FWHM) of the peaks that are resolved with FTNMR. As shown in Figure 1.11.

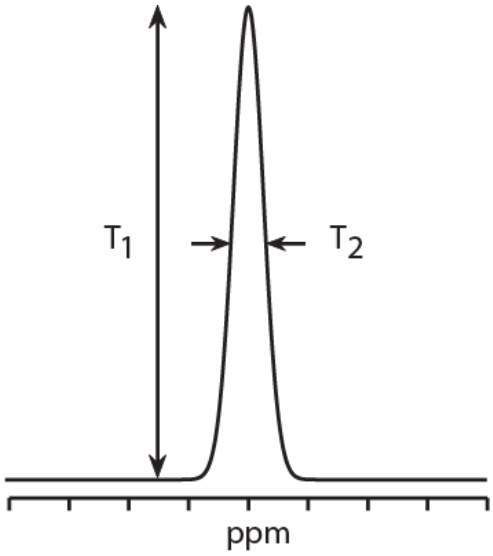

Figure 1.11: T_1 and T_2 are related to the height and full width at half max of FTNMR peaks. This is a visual representation of this relationship.

T_1 and T_2 values cannot be readily quantified from the height and width of peak in a FTNMR spectrum. The T_1 and T_2 can be compared across peaks within a spectrum. These parameters are not just qualitatively related to the FT spectra. Relaxometry parameters have defined mathematical relations to FTNMR spectra.

In a perfect system T_2 could be directly calculated from the FWHM of an FTNMR peak [10, 21]. This relation is of course assuming a perfect system. In reality, inhomogeneous line broadening and other factors make the calculation of T_2 from FWHM more difficult as

$$\frac{1}{T_2^{obs}} = \frac{1}{T_2^*} + \frac{1}{T_2} \tag{1.22}$$

where T_2* is the effective transverse relaxation time and T_2^{obs} is the observed T_2 value. The true relation becomes the calculation of the effective transverse relaxation time, T_2*. T_2* accounts for the inhomogeneity of a field and uses the B_{eff} that a spin is actually experiencing. The relation is [6]

$$T_2^* = \frac{1}{\pi \Delta \nu_{1/2}} \tag{1.23}$$

where $\Delta\nu_{1/2}$ is the FWHM of the FT peak in question in the case where $T_2^{obs} \sim T_2^* \gg T_2$. The peak width is measured in frequency units since FTNMR spectra are in the frequency domain after the FT transformation of the time domain data. Equation 1.23 calculates the T_2^* or T_2^{obs} for short T_2 values. Effective T_2 is what can be obtained in this manner given inhomogeneities in magnetic fields.

1.6 How an NMR Assembly works from programming to signal

Next, consider practicalities of obtaining an NMR signal, from the NMR assembly or spectrometer to the probe. Samples for NMR are generally on the mL scale. These samples are placed in, or on, an NMR probe. Then the probe is placed in a magnetic field. The NMR signal is created by sending a rf pulse from a signal generator to the probe. Then signal received from the sample is detected and sent to a computer. Once the sample signal reaches the computer it is processed in the appropriate manner. This process begins and ends with the computer as shown in Figure 1.12 and as now described. Pulse sequences are coded on the computer. When a pulse sequence is run, the computer tells the signal generator to create rf at set frequencies, powers, and durations. The rf pulses are then sent to an amplifier. From the amplifier, the rf pulse is directed to the probe through a duplexer. After the rf pulse is shut off the duplexer directs the low voltage NMR signal to the signal preamplifier and receiver. The duplexer is important since both generated rf and sample signal travel along the same electrical pathway to and from the probe. In the probe, the rf pulse passes through the probe circuit to the coil. When the rf pulse hits the coil, Faraday's law is exploited and a magnetic field, B_1, is generated. The coil is designed so the B_1 field is perpendicular to the external static B_0 field. The B_1 is the magnetic field generated by the inductor. When the B_1 field acts upon the sample in the B_0 field, the spins are perturbed. Once the rf is turned off, the B_1 field will cease to exist. Then the perturbed spins will precess and 'relax' back to alignment with B_0. The precessing

magnetization generates a rf magnetic field that, according to Faraday's law, leads to an electromotive force (EMF) at the amenable NMR signal voltage. The sample signal has much less power than the original generated rf signal and must be amplified. After the receiver the NMR signal is sent through to an analog to digital converter and fully digitized by the computer [9, 21].

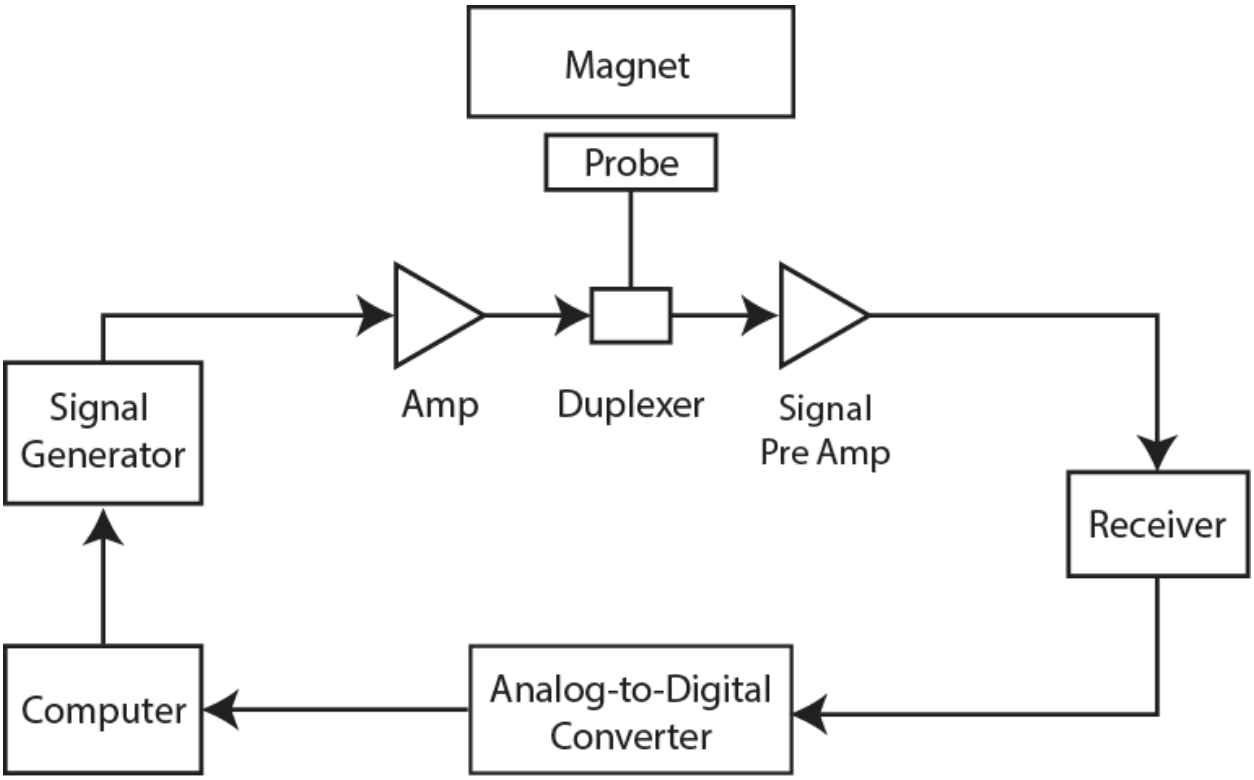

Figure 1.12: Schematic of an NMR set up.

In summary, the computer functions as both the programming tool and the signal processing tool. The signal generator creates rf at the frequency, power, and duration passed to it by the computer. The duplexer discriminates between computer generated signal and sample generated signal and sends each rf in the appropriate direction [26].

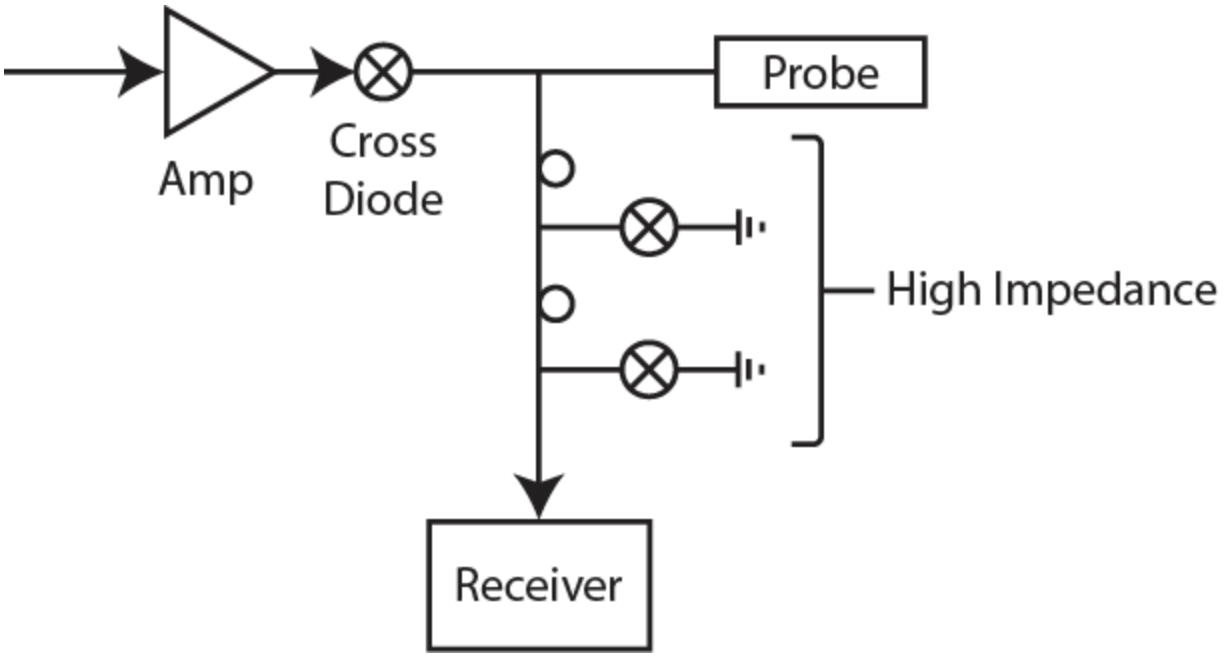

Figure 1.13: Schematic of a duplexer.

Duplexers work as a passive switch [9]. The rf signal comes in with high power from the signal generator. The rf passes through cross diodes and rf is presented with two pathways. One pathway has high impedance, with a set of λ/4 coaxial cross diodes to ground [27] while the other has with low impedance as it is connected to a tuned and matched probe. The generated rf follows the path of least impedance and goes to the probe. The signal coming from the probe is of lower power. The lower power signal is also faced with two pathways at the duplexer. The sample signal cannot achieve the forward biasing voltage of the cross diodes and is sent the out towards the receiver. A schematic of a duplexer can be seen in Figure 1.13.

Faraday's law describes the relationship between EMF and magnetic flux, Φ_B [28]. This relationship explains how the electrical current in the coil inductor can induce a magnetic field. The inverse of that, how magnetic flux induces EMF, describes how signal is detected from the sample.

$$EMF = -\frac{d\Phi_B}{dt} \tag{1.24}$$

Equation (1.24) is the mathematical combination of Faraday's law and Lenz law that describes how magnetic flux over time can induce an electric current. In this case it would be the induction of an electric current in the probe circuit inductor. The EMF induced by the rf generates magnetic flux and thus a magnetic field as it passed through the inductor [26]. The magnetic fluctuations created by spin precession and relaxation induce EMF in the coil.

NMR experiments are made up of a sequence of rf pulses sent from the computer out to the probe. The variations in the rf manipulate spins. Signal generated from the fluctuations in the magnetic field are processed by the computer. The processed data is used to extract relaxation parameters and other relevant data.

1.7 Anatomy of a Probe/How to build a probe

An NMR probe consists of an LC circuit. L stands for inductor and C stands for capacitor. In NMR circuits, the coil is used as the inductor. In order to maximize the signal obtained, the probe circuit must be tuned and matched. The circuit is tuned to the frequency of interest and matched to 50 Ω [27]. The frequency of interest is chosen based on the Larmor frequency of the target nucleus. Larmor frequencies of nuclei vary with magnetic field strength. Thus, the frequency of interest is chosen by a combination of field strength and nucleus of interest. The circuit impedance is set to 50 Ω so that it matches the resistance of the coax cables carrying the rf signal. The impedance must be matched in order to minimize reflection, and thus to get the maximum signal amplitude. The more signal the more information can be obtained from an experiment. The probe coil must also be the correct shape and orientation for the magnet assembly that will be used.

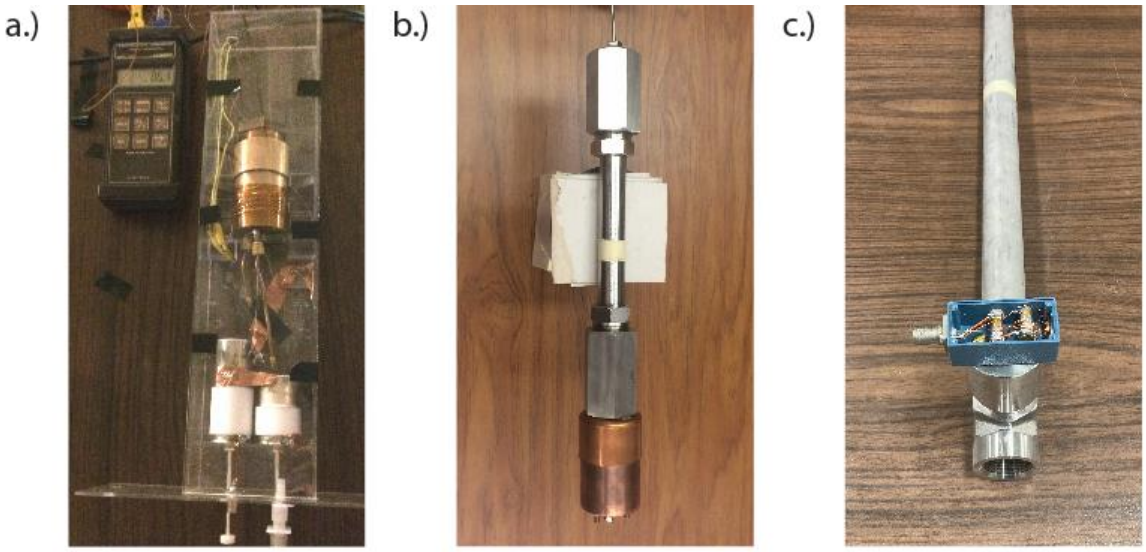

Figure 1.14: Selected examples of NMR probes constructed in this work. (a.) Probe to hold an NMR pressure cell in an MRI assembly. The sample was encased in the pressure cell. (b.) High pressure probe made to interface with multiple magnet assemblies. (c.) NMR probe made out of industrial pipe, developed to interface with an MRI magnet assembly.

Probes can take many forms and commonly need to be developed to solve geometrical limitations of NMR. Some examples are shown in Figure 1.14. Common circuits used in NMR probes are tank circuits, the schematics for two tank circuits are shown in Figure 1.15.

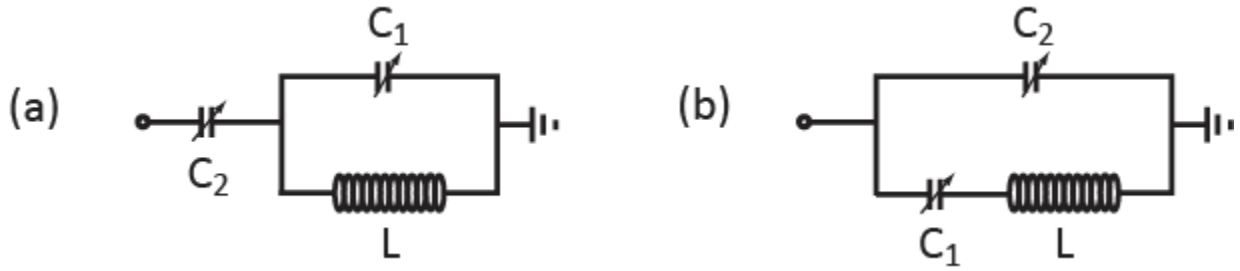

Figure 1.15: Schematics for two tank circuits used in NMR probes. L denotes the inductors and C_n (n=1,2) denotes capacitors.

The resonant frequency of an LC circuit is calculated using the values of the inductors, L, and the capacitors, C. The equation for calculating the resonant frequency, ω, of a LC circuit is [27]

$$\omega = \frac{1}{\sqrt{LC}} \tag{1.25}$$

Indicating that both L and C change ω.

The tank circuits shown in Figure 1.15 work better for different NMR assemblies and magnets. The tank circuit shown in Figure 1.15(a) works better with lower frequencies. The circuit shown in the schematic in Figure 1.15(b) works better for higher frequencies. Typically, lower C values are required to tune and match Figure 1.15(a) at low frequencies. These tank circuits have two capacitors and one inductor each. In the Figure 1.15(b), there is one capacitor involved in tuning the circuit, C_1, and the other capacitor is involved in matching the resistance of the circuit to 50 Ω, C_2. These are considered independent capacitors. In the schematic in Figure 1.15(a) capacitors are interactive. Interactive means that both capacitors are involved in tuning the circuit. Tuning the circuit involves minimizing the impedance of a circuit at the frequency of interest. Math explaining why the capacitors are independent or interactive for tuning and matching is seen in equations (1.26)-(1.32) [29]. It begins with the basic calculations for impedance for circuits, capacitors, and inductors.

For $j = \sqrt{-1}$, the impedance for a series LC circuit is

$$Z = j\omega L + \frac{1}{j\omega C} \tag{1.26}$$

For a parallel circuit of a capacitor and an inductor the inverse impedance is

$$\frac{1}{Z_{parallel}} = \frac{1}{j\omega L} + \mathrm{j}\omega C, \tag{1.27}$$

the equation can easily rearrange to

$$\mathrm{Z_{parallel}} = \frac{j\omega L}{1 - \omega^2 LC} \tag{1.28}$$

The total impedance for the tank circuit in Figure 1.15 (a) is the combination of the parallel circuit with a capacitor added to it

$$\mathrm{Z_a} = \frac{j\omega L}{1 - \omega^2 L C_1} + \frac{1}{j\omega C_2}, \tag{1.29}$$

that equation factors to

$$\mathrm{Z_a} = -j\left(\frac{1 - \omega^2 L(C_1 + C_2)}{\omega C_2(1 - \omega^2 L C_1)}\right) \tag{1.30}$$

The circuit is considered tuned when the impedance goes to zero. The impedance goes to zero when the numerator is zero. Since both C_1 and C_2 are in the numerator, both are involved in tuning and matching of the circuit.

The impedance for the circuit in Figure 1.15 (b) is

$$\frac{1}{Z_b} = \frac{\mathrm{j}\omega \mathrm{L}}{1 - \omega^2 \mathrm{L} C_1} + \mathrm{j}\omega C_2 \tag{1.31}$$

which can be rearranged to

$$Z_b = -j\left(\frac{(1 - \omega^2 L C_1)}{\omega C_2(1 - \omega^2 L C_1) + \omega L}\right) \tag{1.32}$$

In this case, only C_1 is involved in tuning the circuit. C_2 matches the resistance of the circuit to 50 Ω.

In the NMR circuits seen here, the inductor present in the circuit is the coil. Coils can be built for a certain circuit or sample. When a coil is custom built the value of its inductance is important. The inductance of a coil is affected by the number of turns, N, length of coil, l, and cross section of the coil, A, as.

$$\mathrm{L} = \frac{\mu_0 N^2 A}{l} \tag{1.33}$$

where μ_0 is the permeability of free space at $4\pi \times 10^{-6} \frac{m \cdot kg}{s^2 A^2}$. This relation can be used to calculate the number of turns, or length needed when attempting to build a coil to a specific inductance. The diameter, number of turns, and length of the coil can all be important in tuning and matching of a circuit [30].

The quality of the circuit affects the size of the signal voltage and data collected by the circuit. The quality factor, Q [31] is a dimensionless ratio that can be calculated or experimentally measured. The Q factor can be measured from recorded circuit response across a range of frequencies. The response is measured as the reflection coefficient

$$\Gamma = \frac{(Z - 50)}{(Z + 50)} \tag{1.34}$$

with FWHM and position ω_0 related to Q as [31]

$$\mathrm{Q} = \frac{\omega_0}{\mathrm{FWHM}} \tag{1.35}$$

Real resistance, not residual impedance in the circuit, needs to be minimized at the frequency of interest in order to be able detect the strongest signal possible. Real resistance is minimized when the FWHM goes to zero and the Q goes to infinity.

1.8 References

[1] V. M. Balasubramaniam and D. Farkas, "High-pressure food processing.," *Food. Sci. Technol Int.,* no. 14, pp. 413-418, 2008.

[2] M. Muntean, O. Marian, V. Barbieru, G. Cătunescu, O. Ranta, I. Drocas and S. Terhes, "High pressure processing in food industry -- characteristics and applications," *Agric. Agric. Sci. Procedia.,* no. 10, pp. 377-383, 2016.

[3] N. Gosavi, D. Salvi and M. Karwe, "High pressusre-assisted infusion of calcium into baby carrots part 1: influence of process variables on calcium infusion and hardness of the baby carrots," *Food Bioproc Tech,* no. 12, pp. 255-266, 2019.

[4] S. Mahadevan, N. Nitin, D. Salvi and M. Karwe, "High-pressure enhanced infusion: influence of process parameters," *J. Food Process Eng. ,* no. 38, pp. 601-612, 2015.

[5] D. A. McQuarrie and J. D. Simon, Physical Chemistry: A molecular Approach, Sausalito, CA: University Science Books, 1997.

[6] P. Atkins and Julio de Paula, Physical Chemistry: Thermodynamics, Structure, and Charge, Tenth Edition, New York, NY: W.H. Freeman and Company, 2014.

[7] R. K. Harris, Nuclear Magnetic Resonance Spectroscopy, Essex, England: Addison Wesley Longman Limited, 1986.

[8] N. Chandrakumar and S. Subramanian, Modern Techniques in High-Resolution FT-NMR, New York: Springer-Verlag, 1987.

[9] M. H. Levitt, Spin Dynamics: Basics of Nuclear Magnetic Resonance, West Sussex, England: John Wiley & Sons, Ltd., 2001.

[10] C. P. Poole and H. A. Farach, Relaxation in Magnetic Resonance, New York: Academic Press, 1971.

[11] C. P. Slichter, Principles of Magnetic Resonance, Berlin: Springer-Verlag, 1978.

[12] R. A. McQuarrie, Statistical Mechanics, New York: Harper & Row, Publishers, 1973, pp. 72-76.

[13] A. Abragam, The Principles of Nuclear Magnetism, Oxford University Press, 1961.

[14] E. O. Stejskal and J. E. Tanner, "Spin diffusion measurements: spin echos in the presence of a time-dependent field gradient," *J. Chem. Phys.,* vol. 42, no. 1, pp. 288-292, 1965.

[15] F. Bloch, "Nuclear Induction," *Physical Review,* vol. 70, pp. 460-474, 1946.

[16] R. Freeman, A Handbook of Nuclear Magnetic Resonance, Essex: Longman Scientific & Technical, 1987.

[17] H. Y. Carr and E. M. Purcell, "Effects of diffusion on free precession in nuclear magnetic resonance experiments," *Phys. Rev.,* vol. 95, no. 3, p. 630, 1954.

[18] J. L. Markley, W. J. Horesley and K. P. Melvin, "Spin-Lattice Relaxation Measurements in Slowly Relaxing Complex Spectra," *J. Chem. Phys.,* vol. 55, no. 7, p. 3604, 1971.

[19] E. L. Hahn, "Spin Echoes," *Physics Review,* vol. 80, no. 4, pp. 580-594, 1950.

[20] S. Meiboom and D. Gill, "Modified spin-echo method for measuring nuclear relaxation times," *The Review of Scientific Instruments,* vol. 29, no. 8, pp. 688-691, 1958.

[21] P. T. Callaghan, Principles of Nuclear Magnetic Resonance Microscopy, Oxford: Oxford University Press, 1991.

[22] M. N. Martin, B. J. Balcom, M. J. McCarthy and M. P. Augustine, "Noninvasive, nondestructive measurement of tomato concentrate spoilage in large-volume aseptic packages," *Journal of Food SCience,* vol. 84, no. 10, pp. 2898-2906, 2019.

[23] P. Blümler, B. Blümich , R. Botto and E. Fukushima, Spatially Resolved Magnetic Resonance: Methods, Materials, Medicine, Biology, Rheology, Geology, Ecology, Hardware, Wiley, 2008.

[24] S. W. Young, Nuclear Magnetic Resonance Imaging: Basic Principles, Raven Press, 1984.

[25] M. Vlaardingerbroek and J. Boer, Magnetic Resonance Imaging: Theory and Practice, New York: Springer-Verlag, 2003.

[26] E. C. Young, The New Penguin Dictionary of Electronics, Middlesex: Penguin Books Ltd., 1979.

[27] E. Fukushima and S. B. Roeder, Experimental Pulse NMR: A Nuts and Bolts Approach, Reading: Addison-Wesley Publishing Company, 1981.

[28] D. J. Griffiths, Introduction to Electrodynamics, Englewood Cliffs: Prentice-Hall, Inc., 1989.

[29] B. H. Vassos and G. W. Ewing, Analog and Digital Electronics for Scientists, New York: John Wiley & Sons, 1980.

[30] C.-N. Chen and D. I. Hoult, Biomedical Magnetic Resonance Technology, Bristol: IOP Publishing Ltd, 1989.

[31] R. J. Smith, Circuits, Devices, and Systems, 3rd ed., New York: John Wiley & Sons, 1966, pp. 183-191.

Chapter 2. A Low Cost, Portable NMR Probe for High Pressure, MR Relaxometry

2.1 Abstract

A low-cost, portable, high-volume, stainless steel pressure reactor is modified to easily perform magnetic resonance relaxometry at industrially relevant pressures. Unlike existing pressurization strategies common to nuclear magnetic resonance (NMR) spectroscopy, this approach is amenable to realistic samples that feature heterogeneity and have traditionally escaped NMR study at pressure. This pressure reactor/NMR probe combination is easily accommodated by most single-sided and other low magnetic field permanent magnet assemblies. The performance of the probe is demonstrated by accomplishing NMR relaxometry on polydimethylsiloxane at different pressures with two types of unilateral magnets.

2.2 Introduction

Liquid- and solid-state nuclear magnetic resonance (NMR) spectroscopy have enjoyed a rich history in the characterization of material properties and chemical transformations at elevated pressure. The pioneering work of Jonas in the development of NMR probes with hydraulic-based pressure cells enabled the initial NMR characterization of liquids at pressures up to 900 MPa [1]. Originally this type of high-pressure NMR research was restricted to those with access to the pressurization apparatus and NMR probes of the Jonas design [1-3]. The situation has improved in the past few years as Daedelus Innovations improved on the Jonas approach to produce a commercially available pressure cell and necessary pressurization hardware [4]. The Daedelus device uses a zirconia cell to replace a standard 5 mm NMR tube that can be accommodated by most high-resolution NMR probes, a feature that led Wand to study pressure recyclable protein folding with high resolution NMR [5]. The protein folding work is remarkable,

but the time scale of pressurization limits the study to equilibrium chemical structure changes with and without added pressure [6]. Recently, Bax replaced the low-volume syringe-pump pressurization apparatus with a large volume bellows system to enable the zirconia cell enclosed sample pressure to drop by ca. 200 MPa in ca. 2 ms, thus allowing the measurement of real-time pressure-induced folding dynamics by NMR [7].

The hydraulic-based pressurization strategies are limited to pressures below about 900 MPa [1] which is adequate for protein-folding research, but far too low to study other problems requiring much higher pressure, like aqueous phase geochemistry [8,9]. To achieve these higher pressures, mechanical force is used. For liquids, Casey developed a clamp cell based NMR probe capable of delivering high resolution, two dimensional, liquid-state NMR spectra for solutes in water or organic solvent at pressures up to 3 GPa [10]. Simple modifications to the coil orientation and the exotic alloys used in the probe construction will easily increase the operating pressure upper limit to 5 GPa. An attractive feature of the clamp cell design is that the sample volume is kept ca. 1 mL, thus examination of solute and heteronuclei NMR spectra at pressures up to 5 GPa is possible. Two orders-of-magnitude higher pressure has been mechanically established on nL volume samples with diamond anvil cells modified for NMR spectroscopy [11]. Both the clamp cell and diamond-anvil-based NMR probes are custom built research devices that are not commercially available.

The goal of this work was to develop a low-cost, portable NMR probe capable of studying realistic, heterogeneous, industrially relevant, sometimes reactive, samples at elevated pressure. Realistic samples include food, biomass, drilling muds, etc. that are not usually homogeneously dispersed. Unfortunately, available high-pressure-NMR instrumentation designs are not amenable to this type of research. Current approaches to high pressure NMR have focused on the pressurized space being enclosed in the magnet. Having the pressurized sample enclosed in a magnet assigns a geometric and size limit to the probe and pressurization system. The small physical size requirement translates into the development of delicate,

expensive, equipment with a small sample volume. Other custom approaches have demonstrated that NMR is feasible in conjunction with metallic, high-pressure vessels that have the coils located inside the pressure space with the vessel acting as the ground shield, as discussed below [12,13]. These other approaches are restricted to either lower pressures or specific samples and geometries like cylindrical rock cores [12-14]. The low volume of existing approaches is the first problem. Although adequate for limited quantity biomolecule solutions, the low nL – mL sample volumes of existing NMR pressure cells make the study of many realistic samples at pressure impossible i.e. it is difficult to load an oil sample with small rocks or paste, like guacamole, into a valuable, 3 mm inner diameter, zirconia NMR pressure cell. A second problem is durability. Commercially available and research specific NMR pressure devices are designed for use in academic laboratories where simple two-component clean solutions are used. Industrially relevant dirty mixtures will significantly reduce the lifetime of the existing pressure cells. Finally, there is cost. The Daedelus liquids and the diamond anvil cell solids pressurization hardware involves expensive components, thus much high-pressure research is expensive to accomplish.

The samples of interest to this work are realistic, meaning that they are mixtures of chemical compounds and/or mixtures of liquids and solids. As most of these samples are also industrially relevant, a maximum operating pressure of at most 600 MPa, or 87 Kpsi, is required. This pressure is consistent with the operating pressure of most modern high-pressure food processors [15]. Since such samples often lead to congested, largely uninterpretable NMR spectra there is no need to use expensive, high-resolution magnets for this work. NMR relaxometry, on the other hand, has a rich history in the characterization of realistic samples, does not require expensive magnets and can consequently be accomplished anywhere a portable magnet is placed.

Marble et al., in 2007, introduced a three-magnet array, single-sided portable magnet [16]. The design is simple, small, and compact with a homogeneous sweet spot ca. 1 cm from the magnet surface. In 2014, García-Naranjo et al. showed that this magnet array could be used in conjunction with a solenoid

coil to produce reliable relaxometry measurements on rock core samples with elongated, challenging geometries. Utsuzawa and Fukushima in 2017, described an alternative cylindrical unilateral magnet that uses a magnetic-field saddle point to create adequate field homogeneity. This cylindrical barrel magnet was used to obtain T_1-weighted magnetic resonance images of whole coconuts and to track tomato concentrate spoilage in sealed 1000 L containers [18]. These efforts demonstrate that portable NMR reliably accommodates challenging, non-traditional sample geometries. This work considers adapting commercially available pressure reactors to two portable single-sided magnets to accomplish variable pressure MR relaxometry. Some advantages of this approach are that temperature and flow can be easily controlled and introduced.

The pressure reactors from High Pressure Equipment Company (HiP) are inexpensive, readily available, and specifically designed to study realistic samples at pressures up to 1000 MPa. The following pages describe how a HiP, MS – 17 micro series pressure reactor is modified with a drill and simple components to make a robust, durable, low-cost NMR probe to accomplish pressure-dependent relaxometry with portable magnets. After describing these modifications, the performance of the new HiP-NMR probe is demonstrated by measuring ^{1}H relaxation time correlation data as a function of pressure for polydimethylsiloxane (PDMS) with two different unilateral, single-sided magnets.

2.3 The HiP-NMR Probe

The key design feature that allows for simple modification of a commercial off-the-shelf pressure reactor for NMR measurements is a mixture of Stycast epoxy with Al_2O_3 powder. Since this mixture reliably seals small NMR detection coil lead holes in Berylco-25 alloy up to applied pressures of 3 GPa, the same approach is used here. A standard 316 stainless steel MS – 17 micro reactor, essentially a 1 inch outer diameter, 9/16 inch inner diameter stainless steel tube with threaded ends, and two stainless steel endcaps were purchased from HiP. One of the stainless steel endcaps (Part No. 20-21-LF16-NFB)

interfaces to a syringe pump and is 1/4 inch NPT tapped to receive a male 1/4 inch NPT threaded pressure transmission line. One 1.18 mm diameter hole was drilled completely through the long axis center of other solid endcap (Part No. 20-21-LF16-C) to allow NMR tank circuit access to the pressure space. Four more shallow holes were drilled on the outer circumference of the stainless steel endcap and 10-32 tapped to connect the 2 inch copper pipe endcap and cylindrical pipe section that houses the NMR detection circuit capacitors.

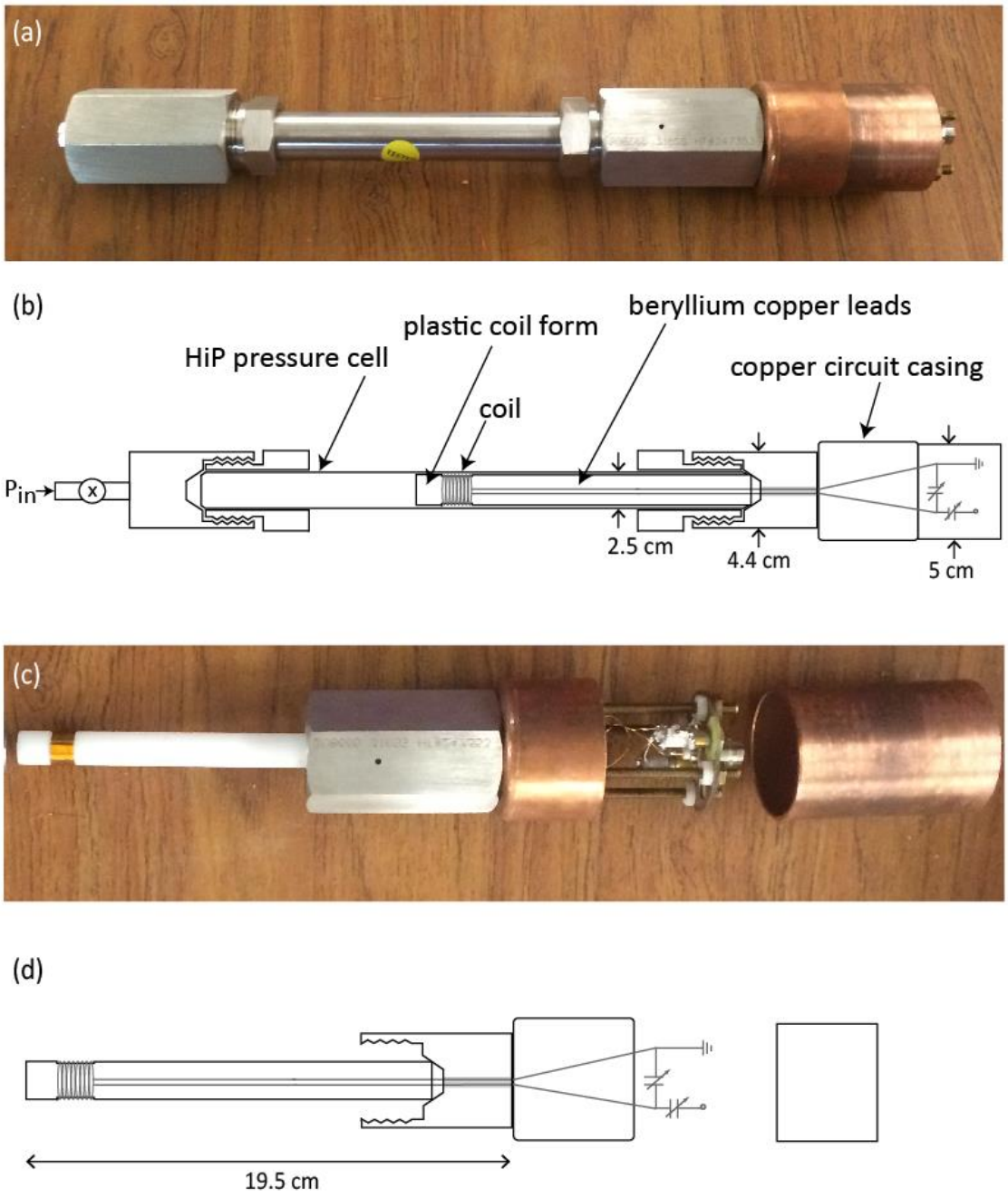

Figure 2.1: Schematics and pictures of the HiP-NMR probe. The stainless steel HiP pressure reactor is on the left and the added copper NMR circuit ground shield is on the right in the photograph of the HiP-NMR probe shown in (a). A schematic of the probe showing the plastic coil sleeve is provided in (b). The Berylco – 25 coil, plastic sleeve, and NMR detection circuit in the photograph in (c) are drawn in the schematic (d).

A photograph of the HiP-NMR probe showing the HiP stainless steel reactor with endcaps and the copper NMR circuit housing is provided in Figure 2.1(a). The schematic drawing of the HiP-NMR probe in Figure 2.1(b) shows some relevant dimensions, the HiP reactor and endcaps, the copper pipe containing the capacitors for the NMR circuit, and a press-fit tubular plastic coil form that sleeves into the HiP reactor. The NMR detection coil is mounted at the end of this 1.4 cm outer diameter, 0.94 cm inner diameter tubular plastic coil form as shown in the photograph in Figure 2.1(c) and the schematic drawing in Figure 2.1(d). Coil forms were constructed from several different plastics in anticipation of unwanted background signals and reactivity to chemicals and pressure. To date coil forms made from Teflon, Delrin, and polyvinylchloride performed the same with no evidence of background signals, reactivity to chemicals and deformity due to pressure. The plastic tube length is adjusted so that the NMR detection coil is centered in the pressure reactor and placed close to the wall of the pressure reactor to maximize sample volume inside of the solenoid coil thus improving detected signal amplitude. The solenoid coil is typically wrapped with Kapton tape to prevent electrical arcs to the pressure reactor wall. The 28 gauge, 21 turn, L = 6.8 μH, Berylco – 25 solenoid NMR detection coil has 32 cm long leads threading through and Stycast/Al_2O_3 epoxy sealed into the stainless steel endcap. These leads connect to the capacitors in the copper pipe ground shield to create the NMR tank circuit. Berylco – 25 was used to prevent the extrusion at high pressure commonly observed with copper wire. The consequence of this choice is that the coil plus lead resistance R = 3.4 Ω is extremely high and thus the circuit quality factor Q is low in comparison to using copper to construct an identical NMR detection coil with long leads.

Before putting the HiP-NMR probe near any human beings and delicate instrumentation it is important to make sure the pressure reactor can still be safely operated at the target pressures. Safety testing is a critical effort because the hole drilled in the pressure reactor end cap violates any safety information for the pressure reactor provided by HiP. Experience dealing with these modifications to HiP

pressure reactors reveals that the reactor can safely maintain pressure up to 80 % of the HiP maximum quoted operating pressure.

2.4 Materials and Methods

The pure polydimethylesiloxane (PDMS) or Dow Corning® 200 Fluid with 50 CS was used as received from Dow Corning. Stycast epoxy was obtained from Lake Shore Cryotronics, Inc.

Application of the NMR pulse sequences shown in Figure 2.2 and acquisition of the associated transient signals were accomplished using a Tecmag Redstone NMR spectrometer.

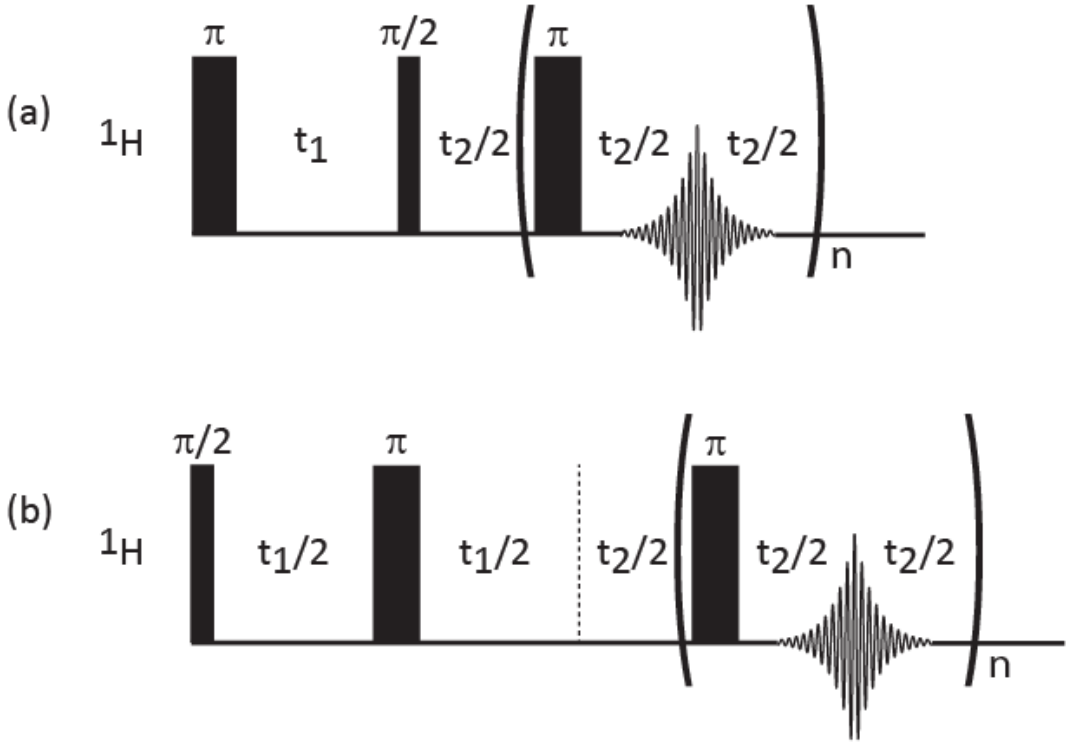

Figure 2.2: Timing diagrams for the NMR pulse sequences. The coupling of the inversion recovery with the CPMG pulse sequence in (a) and the spin echo with the CPMG pulse sequence in (b) respectively provided ^{1}H T_1/T_2^{cpmg} and T_2^{echo}/T_2^{cpmg} correlation data as a function of pressure for this work.

The timing diagram shown in Figure 2.2(a) combines an inversion recovery and Carr-Purcell-Meiboom-Gill (CPMG) pulse sequence together to correlate T_1 with T_2^{cpmg} while the timing diagram shown in Figure 2.2(b) combines the two – pulse spin echo and CPMG pulse sequences together to correlate T_2^{echo} with T_2^{cpmg}. These two pulse sequences were used to track the correlation of these parameters as a function of pressure for ^{1}H nuclei in PDMS at two different magnetic field strengths and geometries. In both of these experiments, 200 acquisitions for each t_1 point were averaged and a 7.1 μs long, $\pi/2$ radio frequency (rf) pulse along with n = 1,000, π rf pulses separated by dt_2 = 820 μs and detection of the spin echo maximum with 40 digitized points sampled every dt_3 = 6.3 μs were used. The T_1/T_2^{cpmg} pulse sequence in Figure 2.2(a) used 40 t_1 points with a dt_1 = 30 ms dwell time while the T_2^{echo}/T_2^{cpmg} pulse sequence in Figure 2.2(b) used 40 t_1 points with dt_1 = 2 ms. A 3.5 s recycle delay was used in all pulse sequences to ensure that the magnetization recovered to thermal equilibrium prior to each scan and to avoid sample heating by reducing the RF-on duty cycle to 0.3 % in these experiments.

Two magnets were used in this study because they are the ideally suited for portable NMR using non-traditional probe geometries like the new HiP-NMR probe. One magnet is a 107 mT, 1.5 cm standoff, single-sided, linear magnet array with an associated 4.57 MHz ^{1}H Larmor frequency [17] while the other is a 123 mT, 1.8 cm standoff, single-sided, cylindrical magnet array with an associate 5.25 MHz ^{1}H Larmor frequency [18].

Pressure was established inside of the NMR probe with a homebuilt syringe-pump pressure system created from commercially available HiP parts. The system uses two in-line transducers to measure and monitor the pressure generated and stored in the pressure system and the HiP-NMR probe. All pressures are within ± 2 % of the quoted value. Caution must be used in the choice of pressure

transmission fluid to avoid sample miscibility issues. Water was used as the pressure transmission fluid for all experiments reported here.

All calculations and data processing were accomplished with laboratory developed Matlab software.

2.5 Results

The photographs in Figure 2.3 show the HiP-NMR probe interfaced to the two magnets used in this study. ^{1}H NMR data were obtained using the linear magnet array in Figure 2.3(a) or the cylindrical magnet array in Figure 2.3(b).

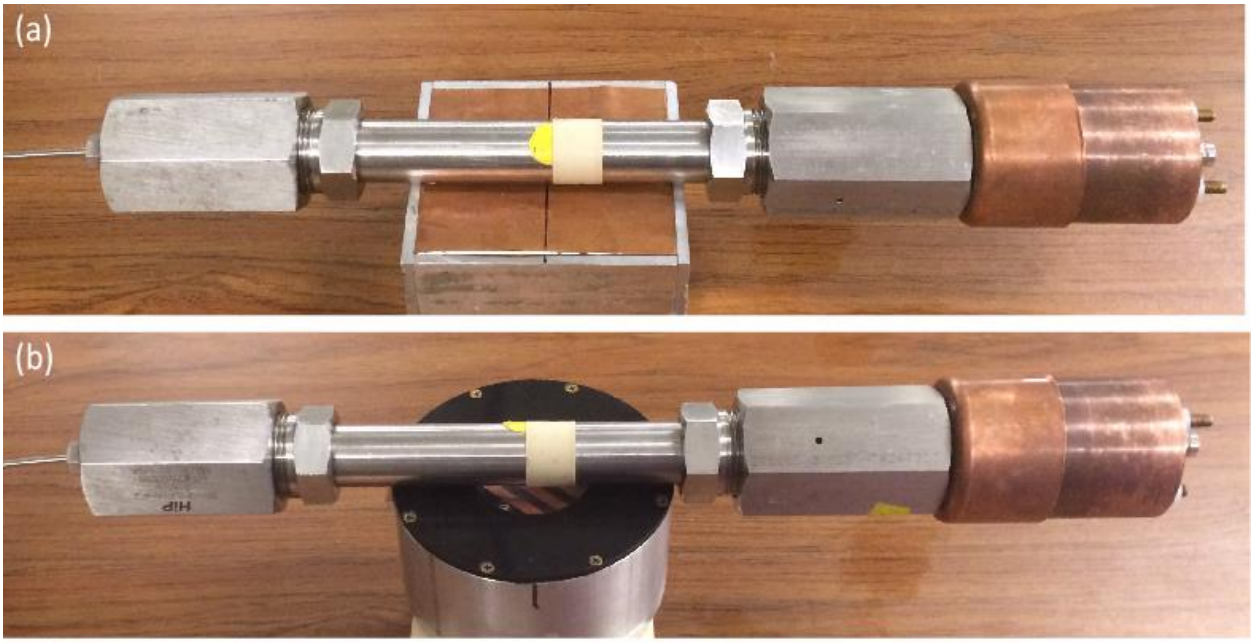

Figure 2.3: HiP-NMR probe with unilateral magnets. The HiP-NMR probe is easy to use. Simple placement on the linear magnet array in (a), or on the cylindrical magnet array in (b) leads to measurable signals.

All NMR experiments were performed at radio frequencies between 4.6 and 5.3 MHz. The high resistance of the Berylco – 25 wire yields a circuit quality factor of Q = 6.6 as measured from the reflection coefficient in the usual way [19]. Despite having such a low Q value, the circuit has surprising rf power handling

efficiency and delivers reasonable signals as typically 80 W of rf power yields a 7.1 μs π/2 rf pulse width and only modest signal averaging is required to obtain useful signal – to – noise ratios.

Examples of two-dimensional ^{1}H relaxation correlation plots obtained using the HiP-NMR probe loaded with PDMS and pressurized to 100 MPa are provided in Figure 2.4.

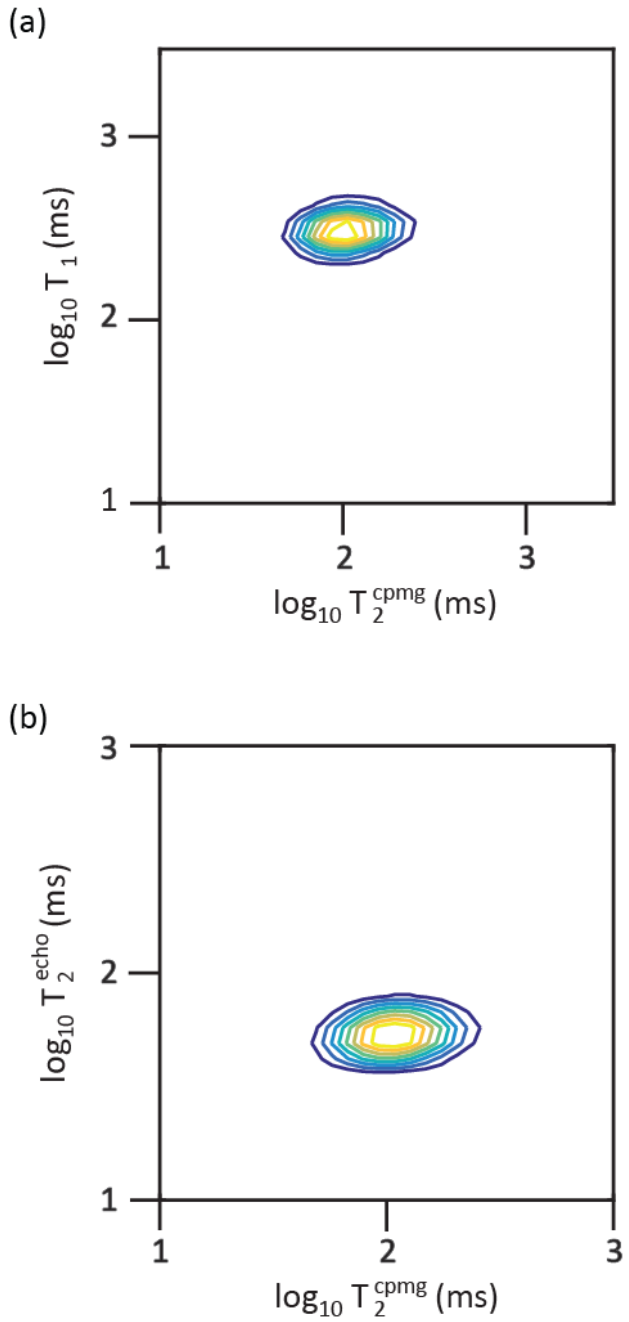

Figure 2.4: Two-dimensional ILT-processed ^{1}H relaxation correlation data. These PDMS data sets were obtained using the linear magnet array at 100 MPa pressure. The ILT is used to convert the raw transient signals produced by the pulse sequences in Figs. 2(a) and (b) to the respective T_1/T_2^{cpmg} and T_2^{echo}/T_2^{cpmg} correlations in (a) and (b).

The T_1/T_2^{cpmg} correlation shown in Figure 2.4(a) was generated by applying a two-dimensional inverse Laplace transform (ILT) to transient signals created with the pulse sequence in Figure 2.2(a). A two dimensional ILT of the transient signals provided by the pulse sequence in Figure 2.2(b) yields the T_2^{echo}/T_2^{cpmg} correlation shown in Figure 2.4(b). Regardless of unilateral magnet or pressure choice, application of the pulse sequences in Figure 2.2(a) and (b) to PDMS always generated just one peak following a two dimensional ILT. Summaries of the pressure and magnet dependence of the T_1/T_2^{cpmg} and T_2^{echo}/T_2^{cpmg} cross-peak position are provided in Figure 2.5 and Figure 2.6 respectively.

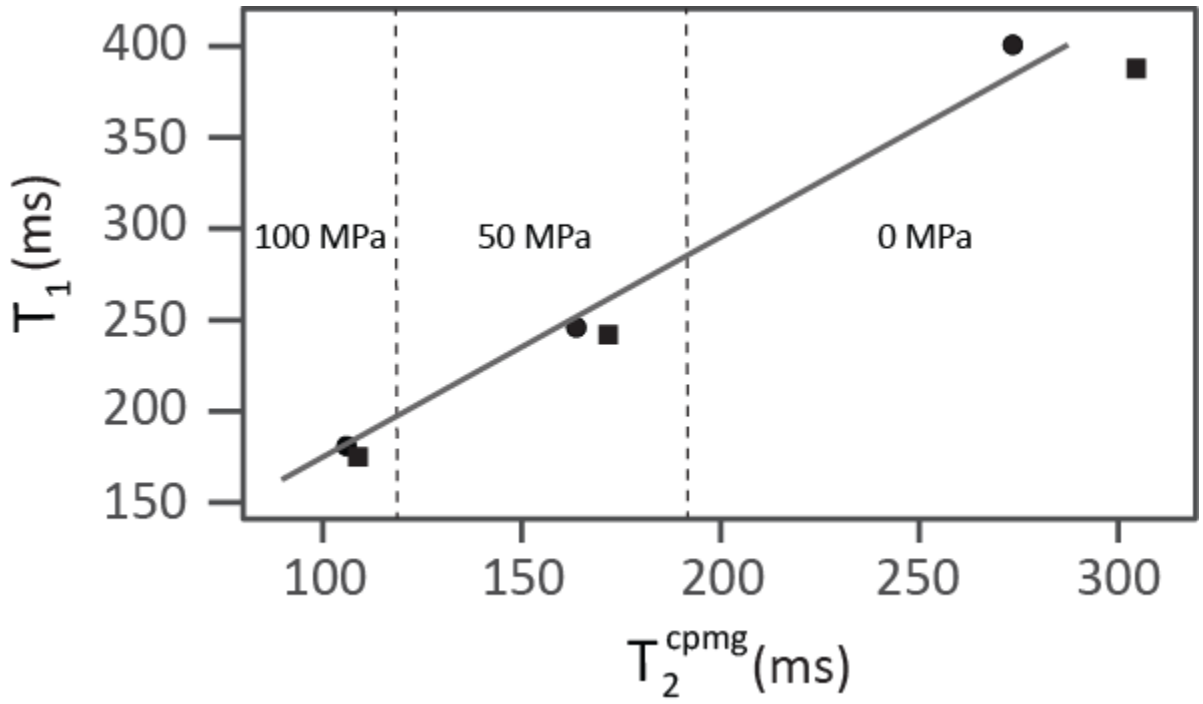

Figure 2.5: Summary of the ^1H T_1/T_2^{cpmg} cross-peak position in PDMS as a function of pressure and magnet. The squares and circles respectively correspond to measurements obtained from the linear and cylindrical magnet arrays. The gray line is included as a guide to the eye.

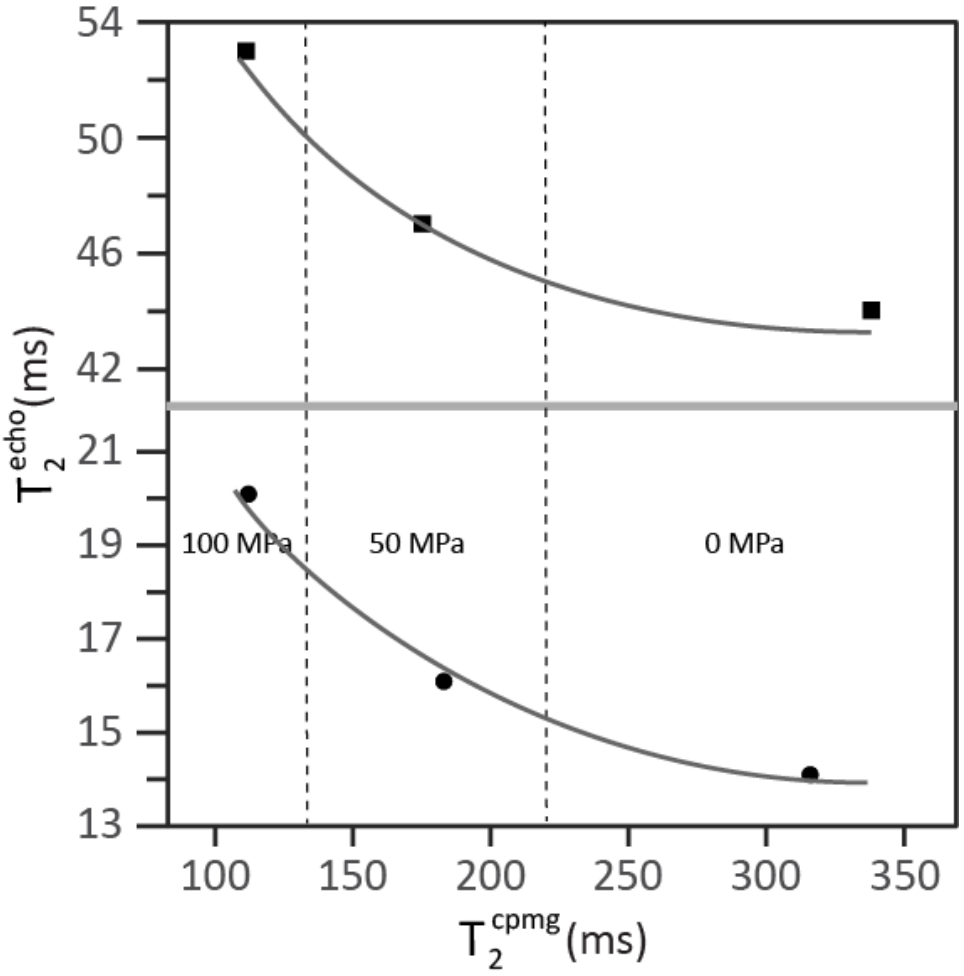

Figure 2.6: Summary of the ^1H T_2^{echo}/T_2^{cpmg} cross-peak position in PDMS as a function of pressure and magnet. The squares and circles respectively correspond to measurements obtained from the linear and cylindrical magnet arrays. The gray lines are included as a guide to the eye.

The square and circle icons in these plots label the cross peak position observed with the linear magnet array in Figure 2.3(a) and the cylindrical magnet array in Figure 2.3(b) respectively. Since there is just one peak in all of the two-dimensional relaxation-correlation plots a simple two-dimensional exponential fit was used to more accurately determine the cross peak position. This analysis approach produced the cross peak positions shown in Figure 2.5 and Figure 2.6.

2.6 Discussion

The HiP-NMR probe design is simple and can be built from commercially available parts and standard non – magnetic capacitors common to an NMR laboratory. Moreover, the probe can be used in any magnet system as long as the HiP reactor fits in the magnet and the static magnetic field is directed perpendicular to the symmetry axis of the NMR detection solenoid coil and long axis of the pressure reactor. This study considered portable unilateral magnet geometries that fulfill these requirements. Helmholtz geometry electromagnets and permanent-magnet-based magnetic-resonance-imaging instruments fulfill both these requirements as well. Although the bore diameter of standard cryogenically cooled solenoid magnets used for NMR spectroscopy may in certain cases accommodate the HiP-NMR probe, the static magnetic field direction is parallel to the long axis of the pressure cell making excitation and detection of traditional NMR signals impossible. One could replace the solenoid coil in the current HiP-NMR probe with a Helmholtz, split-solenoid or a modified Alderman-Grant coil that places the rf field perpendicular to the long axis of the pressure cell in order to interface with a cryogenic solenoid magnet. Although the lower inductance of the coils used in this modified design would be easier to tune at the higher Larmor frequencies common to cryogenic magnets, the rf field would be seriously attenuated by the production of eddy currents in the ground shield that is in near physical contact with the rf coil. In contrast, the same effect can focus and enhance the rf field in the sample when a solenoid coil is parallel to the long axis of the pressure reactor.

It is surprising that the primary limitation in the overall probe design is not the 316 stainless steel used to construct the entire HiP pressure reactor. To date, there have been no problems with either signal acquisition from samples in the pressure reactor or from the HiP-NMR probe magnetizing and becoming stuck in or on an NMR magnet. Presumably this is because 316 stainless steel is largely non – magnetic unless elevated to high temperature by machining. In the cases reported here the strongest part of the

magnetic field is across the center of the pressure reactor tube far from the machined endcaps and threads. In this way the most magnetically susceptible pressure reactor parts are kept in relatively low to zero magnetic field as shown by the photographs in Figure 2.3. The primary limitation of the HiP-NMR probe is related to the use of Berylco-25 wire for the NMR detection coil and the ca. 32-cm-long leads between the NMR tuning capacitors and the NMR detection coil mounted in the center of the pressure space and shown in Figure 2.1(d). Berylco – 25 wire was chosen for one reason as mentioned above. A mixture of Stycast epoxy and Al_2O_3 maintains a pressure seal for a 28 gauge Berylco – 25 wire threading through a 1.8 mm diameter hole in stainless steel, tungsten carbide or beryllium copper alloy up to 3 GPa [10]. The consequence of this choice is that the coil – plus – lead resistance climbs to 3.4 Ω and the circuit quality factor drops to Q = 6.6. The poor Q value is not a problem for NMR excitation as 7.6 μs ^{1}H $\pi/2$ pulses are possible.

The high resistance of the Berylco – 25 wire impacts the experiment in two ways. First, most of the 80 W of applied rf power is being dropped into the 3.4 Ω wire resistance thus local sample heating is possible. Care must be taken to make sure the pulse duty cycle is low enough to prevent this effect. This is not a problem for most protonated samples of interest where T_1 is typically greater than 100 ms. Second, the high wire resistance reduces the reception of the NMR free precession signal as the measured signal voltage is proportional to Q. It was recently shown that 28 gauge enameled copper wire Stycast epoxy/Al_2O_3 sealed into a 1.18 mm diameter hole in beryllium-copper alloy resists extrusion up to 800 MPa [8]. Since the maximum operating pressure of the Micro Reactor family of HiP products is at most 450 MPa a new endcap/coil form assembly is being constructed with 28 gauge enameled copper wire. This alone will drop the wire resistance by a factor of five, and increase the Q by a factor of five thus decreasing the rf power demand and thermal dissipation while increasing the measured NMR signal intensity. The long leads between the NMR circuit capacitors and the NMR detection coil are not desirable, but were chosen because of simplicity and the fact that extra lead inductance does not

introduce circuit tuning issues at Larmor frequencies below 10 MHz. Other coil coupling strategies were considered such as mounting the capacitors directly on the coil, inductively coupling to a remote coil and resonating the pressure reactor itself. It was decided that these other approaches, although superior in some ways, lacked the durability and simplicity known to work in extreme pressure environments and with realistic, heterogeneous, sometimes reactive samples.

The HiP-NMR probe is straightforward to use. Typically, a valve is place between the NPT-threaded pressure-reactor endcap and the syringe pump. Thus, the HiP-NMR probe can be pressurized prior to placement on the single-sided magnets as shown in Figure 2.3(a) and (b). Although this approach may be more desirable as the estimate of real-time pressure dependent dynamics by NMR is made possible, it can be problematic from a signal detection point of view. The HiP pressure reactor also serves as the HiP-NMR probe ground shield. Operation of the HiP-NMR probe with the syringe pump connected introduces noise at certain frequencies. In these cases, additional effort must be placed on the removal of ground loops between the NMR spectrometer, pressure transducers, and other associated electronics as well as making sure all components share a common direct path to ground.

Despite the low Q value of the NMR detection circuit due to Berylco – 25 wire, the HiP-NMR probe was more than able to provide useful relaxometry data. Two NMR experiments at three different pressures were performed on PDMS in order to demonstrate the function, performance, and potential usefulness of the HiP-NMR probe. PDMS is an ideal sample for this work. It is a known lubricant with pressure-dependent macroscopic properties and a reasonable proton density and spin lattice relaxation time that yields a strong signal with minimal signal averaging.

2.6.1 T_1/T_2^{cpmg} ^1H Relaxation Correlation in PDMS

As mentioned above, application of the pulse sequence in Figure 2.2(a) to a sample of PDMS at 100 MPa applied pressure leads to the correlation between PDMS ^1H T_1 and T_2^{cpmg} values following an

ILT as shown in Figure 2.4(a). This data was recorded using the linear magnet array. The plot in Figure 2.5 shows the T_1/T_2^{cpmg} cross peak position as a function of pressure for the two different unilateral magnets. The gray line is included to guide the eye and illustrate that at all pressures $T_1 \approx T_2^{cpmg}$. Closer inspection reveals that at all pressures T_1 is slightly greater than T_2^{cpmg}, suggesting that the static field gradients established by both unilateral magnets are so large that the dt_2 = 820 μs CPMG π pulse delay is too long to completely remove all diffusion contributions to T_2^{cpmg}. The discrepancy between T_1 and T_2^{cpmg} is larger for the cylindrical magnet array than for the linear magnet array suggesting that the persistent static-magnetic-field gradient for the cylindrical array is greater than for the linear array. The fact that $T_1 \approx T_2^{cpmg}$ suggests that the extreme narrowing limit applies and that the correlation time of the motion τ_c is less than the inverse of the Larmor frequency $\tau_c < 1/\omega_0$ at all pressures. The decrease in T_1 and T_2^{cpmg} values with pressure is also expected. As pressure increases, the PDMS viscosity and τ_c also increase. Since, in the extreme narrowing limit $T_1 \approx T_2^{cpmg} \propto 1/\tau_c$, the T_1 and T_2^{cpmg} values decrease with added pressure.

2.6.2 T_2^{echo}/T_2^{cpmg} ^{1}H Relaxation Correlation in PDMS

As mentioned above, application of the pulse sequence in Figure 2.2(a) to a sample of PDMS at 100 MPa pressure leads to the correlation between PDMS ^{1}H T_2^{echo} and T_2^{cpmg} values following an ILT as shown in Figure 2.4(b). This data was recorded using the linear magnet array. The plot in Figure 2.6 shows the behavior of the T_2^{echo}/T_2^{cpmg} cross peak position as a function of pressure for the two unilateral magnets. Again, the gray lines are included to guide the eye. As expected with reference to Figure 2.5, the T_2^{cpmg} value in Fig. 6 drops with pressure in the same way suggesting that the PDMS viscosity increases with pressure since the extreme narrowing limit applies and $T_2^{cpmg} \propto 1/\tau_c$. The increase in the T_2^{echo}

value with pressure on both magnets is also consistent with increased PDMS viscosity with pressure. The value of T_2^{echo} intimately depends on static-magnetic-field-gradient strength and macroscopic diffusion. The attenuation of diffusion effects enjoyed by T_2^{cpmg} due to the application of many π rf pulses is not shared by T_2^{echo} where just one π rf pulse is applied. The greater difference between T_1 and T_2^{cpmg} values obtained using the cylindrical magnet array in Figure 2.5 that was attributed to a larger static-magnetic-field gradient for the cylindrical magnet array versus the linear magnet array is much more pronounced in the magnet dependence of T_2^{echo} values at all pressures in Figure 2.6. The increase in T_2^{echo} values obtained with both magnets with pressure is consistent with increased viscosity at pressure. The increased pressure lowers the macroscopic diffusion coefficient, attenuating the effect of diffusion on the spin echo amplitude thus increasing T_2^{echo}. The idea that the static-magnetic-field gradient is larger for the cylindrical magnet array than for the linear magnet array is illustrated by the nearly a factor of two difference between T_2^{echo} values obtained from these magnets at all pressures.

2.7 Conclusion

The design, construction, and performance of a simple NMR probe capable of studying the pressure dependence of the fundamental NMR relaxometry parameters for realistic, heterogeneous samples was described. The HiP-NMR probe simplicity, dependence on readily available parts, and ability to conform to many portable magnet geometries, provides a low cost avenue to the characterization of many industrial processes at elevated pressure such as high-pressure food processing and the downhole performance of oil well drilling muds. The primary limitation of the current HiP-NMR probe is the use of Berylco – 25 wire that lowers the NMR detection circuit Q and thus the detected signal intensity. Another version of the HiP-NMR probe, currently under construction, replaces this wire with enameled copper to increase the circuit Q and probe sensitivity. Although not stable to 3 GPa, the use of copper wire should

not be problematic until 800 MPa, a pressure above the maximum operating pressure of this family of HiP pressure reactors. Ongoing work involves using NMR relaxometry, portable magnets and the HiP-NMR probe to study industrially relevant samples like high pressure processed foods, oil well drilling mud, and consumable materials at pressure like shaving cream. Hopefully, this simple HiP-NMR probe design will make these types of samples, and others not yet identified, accessible to an inexpensive NMR study for the first time.

2.8 References

[1] L. Ballard, C. Reiner, J. Jonas, High-resolution NMR probe for experiments at high pressures, J. Magn. Reson. A 123 (1996) 81–86.

[2] J. Jonas, Nuclear Magnetic Resonance Measurements at High Pressure, Rev. Sci. Instrum. 43 (1972) 643-649.

[3] J. Jonas, P. Kozoil, X. Peng, C. Reiner, D.M. Campbell, High resolution NMR spectroscopy at high pressures, J. Magn. Reson, B 102 (1993) 299-309.

[4] Daedelus Innovations. http://www.daedalusinnovations.com

[5] J. L. Urbauer, J. H. Short, L. K. Dow, A. J. Wand, Structural analysis of a novel interaction by calmodulin: high-affinity binding of a peptide in the absence of calcium, Biochemistry, 34 (1995) 8099-8109.

[6] R. W. Peterson, A. J. Wand, Self-contained high-pressure cell, apparatus, and procedure for the preparation of encapsulated proteins dissolved in low viscosity fluids for nuclear magnetic resonance spectroscopy, Rev. Sci. Instrum. 76 (2005) 094101-1-094101-7.

[7] C. Charlier, T. R. Alderson, J. M. Courtney, J. Ying, P. Anfinrud, A. Bax, Study of protein folding under native conditions by rapidly switching the hydrostatic pressure inside an NMR sample cell, Proc. Natl. Acad. Sci., 115 (18) E4169-E4178.

[8] B. G. Pautler, C. A. Colla, R. L. Johnson, P. Klavins, S. J. Harley, C. A. Ohlin, D. A. Sverjensky, J. W. Walton, W. H. Casey, A high-pressure NMR probe for aqueous geochemistry, Angew. Chem. 126 (2014) 9946–9949.

[9] G. Ochoa, C. D. Pilgrim, M. N. Martin, C. A. Colla, P. Klavins, M. P. Augustine, and W. H. Casey, ^{2}H and ^{139}La NMR spectroscopy in aqueous solution at geochemical pressures, Angew. Chem. 127 (2015) 15664–15667.

[10] M.P. Augustine, G. Ochoa, W.H. Casey, Steps to achieving high-resolution NMR spectroscopy on solutions at GPa pressure, Am. J. Sci., 317 (2017) 846-860.

[11] S-H Lee, K. Luszczynski, R. E. Norberg, NMR in a diamond anvil cell, Rev. Sci. Instrum. 58 (1987) 415-417.

[12] H. Han, M. Ouellette, B. MacMillan, F. Goora, R. MacGregor, D. Green,and B. J. Balcom, High pressure magnetic resonance imaging with metallic vessels, J. Magn. Reson. 213 (2011) 90–97.

[13] R. Freedman, V. Anand, B. Grant, K. Ganesan, P. Tabrizi, R. Torres, D. Catina, D. Ryan, C. Borman, C. Krueckl, A compact high-performance low-field NMR apparatus for measurements on fluids at very high pressures and temperatures, Rev. Sci. Instrum. 85 (2014) 025102-1-025102-10.

[14] M.Shakerian, B. J. Balcom, A MR/MRI compatible core holder with RF probe immersed in containing fluid, J. Magn. Reson. 286 (2018) 36-41.

[15] M. Muntean, O. Marian, V. Barbieru, G.M. Cătunescu, O. Ranta, I. Drocas, S. Terhes, Agric. Agric. Sci. Procedia 10 (2016) 377–383.

[16] A.E. Marble, I.V. Mastikhin, B.G. Golpitts, B.J. Balcom, A compact permanent magnet array with a remote homogeneous field, J. Magn. Reson. 186 (2007) 100-104.

[17] J.C. García-Naranjo, P. Guo, F. Marica, G. Liao, B.J. Balcom, Magnetic resonance core-plug analysis with the three-magnet array unilateral magnet, Petrophysics 55 (2014) 229-239.

[18] S. Utsuzawa, E. Fukushima, Unilateral NMR with a barrel magnet, J. Magn. Reson. 282 (2017) 104-113.

[19] C-N. Chen, D.I. Hoult, Biomedical magnetic resonance technology, Adam Hilger, New York, 1989.

Chapter 3. Using MRI to Study High Pressure Assisted Nutrient Infusion

3.1 Abstract

High-pressure assisted infusion of nutrients into food is monitored *in situ* with magnetic resonance imaging (MRI). Modification of an off-the-shelf pressure reactor with an MRI detection circuit provides a sufficiently large volume to accommodate food. The model food used here is peeled apple flesh, as it is considered a good mimic for fibrous food. The nuclear-spin relaxation properties of the water surrounding the apple flesh are enhanced by adding paramagnetic Mn^{2+}(aq) cations. In this way, MRI relaxation contrast can be used to monitor the location of doped, bulk water in and around the apple flesh during pressurization. Prior to this work, there was not a way to determine efficiencies of pressurization strategies *in situ*. This MRI approach is used to demonstrate that pressure gating and ramping offer no nutrient mass transport advantage over operation at constant pressure and that the presence of a peel expectedly disrupts solute transport into the fruit. High-pressure assisted infusion, with all pressurization strategies shown here, yields at least 50 fold faster infusion times than at ambient pressure.

3.2 Introduction

Increasing the nutritional value of food is a goal of modern food science [1]. This increase can be accomplished with natural hybridization/evolution techniques [2] or genetic modifications [3] prior to growth, by controlling the fertilizers/nutrients provided [4] or the environmental conditions [5] during growth, by using chemistry during manufacturing and processing [6], and finally through preparation prior to consumption [7]. This work considers how high-pressure assisted infusion can be used in the manufacturing and processing step to increase the nutritional content of food. High-pressure assisted infusion is a mechanical technique that places small molecules or nutrients like vitamins or supplements

into food, essentially making 'superfoods' without altering genetic material. With the distrust of genetically modified organisms (GMOs) in the food sector [8], high-pressure assisted infusion presents a pathway to increase the nutritional value of food while maintaining a non-GMO label [9]. This approach was successfully demonstrated in model fruit including the infusion of quercetin into cranberries [10], bioactive compounds into solid apples [11], and calcium into carrots [12]. A particularly nice feature of all this work is that the pressurization systems required to accomplish high-pressure infusion are already used commercially in the food industry for high-pressure food processing [13]. High-pressure food processing is a cold pasteurization technique used to sterilize foodstuff like hummus, guacamole, and baby food [14]. For high-pressure infusion, the fruit is typically placed in a bath containing the nutrients in water and the entire fruit/bath complex is housed in the high-pressure food processor [13]. Application of pressure essentially squeezes the nutrient filled solution into the fruit.

A consequence of using industry standard high-pressure food processors to experimentally understand high-pressure infusion is restricted sample access. Once placed into the pressurization space, the sample cannot be examined until removed. Thus, information regarding mass transport mechanisms involving the infusion of nutrients from the bath into the fruit involves destructive cross sectioning or after removal from the high-pressure food processor. Here, separate fruit cross sections are typically homogenized, extracted with some solvent, and explored with gas or liquid chromatography coupled with mass spectrometry [9,10,12]. By calibrating the instruments to detect the infused nutrient, the cross sectional density of the nutrients is physically determined. Repeating the pressurization for a longer period of time on similarly sized fruit provides a labor intensive estimate of pressure-enabled nutrient transport. Indeed, this approach was used to estimate the pressure-induced diffusion of quercetin into cranberries by Nitin et al. [10].

The purpose of the work reported here is to demonstrate that the combination of a high volume, off-the- shelf pressure reactor modified to accommodate a nuclear magnetic resonance probe circuit [15],

with conventional magnetic resonance imaging (MRI) [16], can be used to study high-pressure nutrient infusion into food. The pressure reactor/probe has already been used to study nuclear spin relaxation at pressures commonly used for high pressure food processing and is a natural choice for this work given the large sample volume [15]. The model fruit used in this study was ca. 1 cm^3 of solid apple flesh and the bulk water surrounding the fruit that typically dissolves the nutrients was doped with manganese chloride, $MnCl_2$. As described below, the Mn^{2+} manganese ions allow the bulk water to be discriminated from the fruit localized water with an MRI measurement. Thus the penetration of this bulk water, that transports nutrients into the fruit, is tracked *in situ* as a function of time at high pressure. Specifically, the model apple system was used along with MRI to determine which of the four pressurization strategies shown in Figure 3.1 most efficiently infuses solution into the apple flesh.

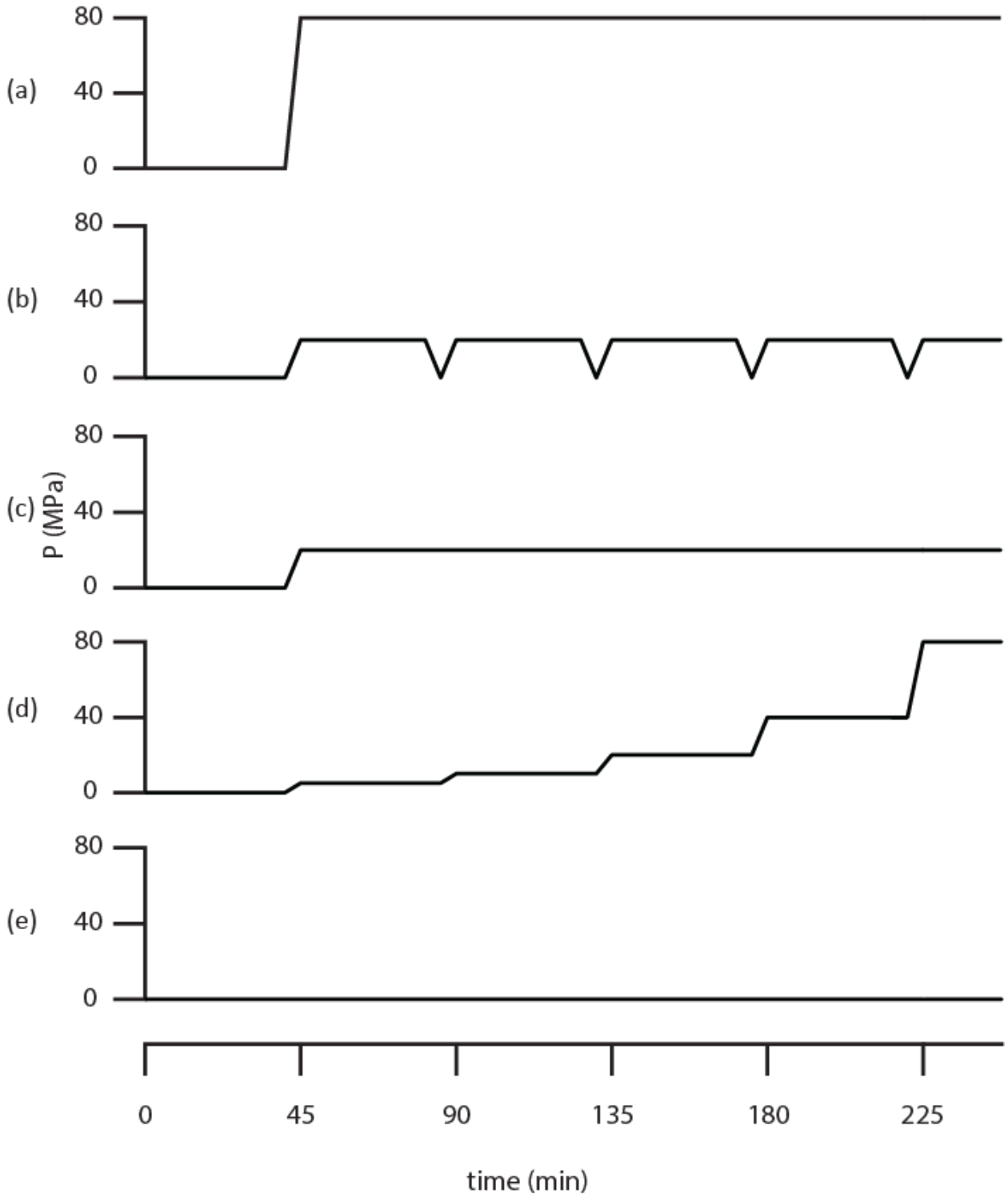

Figure 3.1: Timing diagram comparing the static 80 MPa pressure in (a), cycled 20 MPa pressure in (b), static 20 MPa pressure in (c), ramped pressure up to 80 MPa in (d) and ambient pressure in (e) pressurization strategies. Each pressurization run typically lasted 4.5 hours while the pressure changes indicated in the diagram, that include a 5 minute equilibration period, lasted roughly 10 minutes.

3.3 MRI as a Non-invasive Penetrometer

Magnetic resonance imaging is a useful non-invasive way to explore the proton density inside of an object [17]. This fundamental property is why MRI is so useful in medicine. The proton or water density of bone is smaller than in muscle or blood, thus a spatial estimate of this density provides a pixel-by-pixel picture of human anatomy [18]. The intensity of an MRI image pixel depends primarily on proton density, but in the case where drastically different spin relaxation times are present, can also depend on these times [19]. This feature of MRI is exploited in this work by completely immersing the apple flesh into doped water. Mn^{2+} doped water has drastically decreased relaxation times due to the five unpaired electrons in the Mn^{2+} ion [17]. In this way, the doped water can act as an MR contrast reagent. Here the relaxation time for water in the apple flesh is often in excess of 1.5 s while the ca. 1 mM Mn^{2+} solutions yielded the much shorter ca. 150 ms long value. By performing the MRI pulse sequence with a very short recycle delay the long-lifetime apple-flesh-based water signal is eliminated from the image while the shorter lifetime, external, Mn^{2+} doped, bulk-water signal is displayed [18,19]. In this way the apple, or region of interest, appears as a negative space image. It stands to reason that these dark images will become lighter for long times at ambient pressure or shorter times at elevated pressure due to transport of the doped water into the apple flesh. The left hand column in Figure 3.2 graphically describes this process.

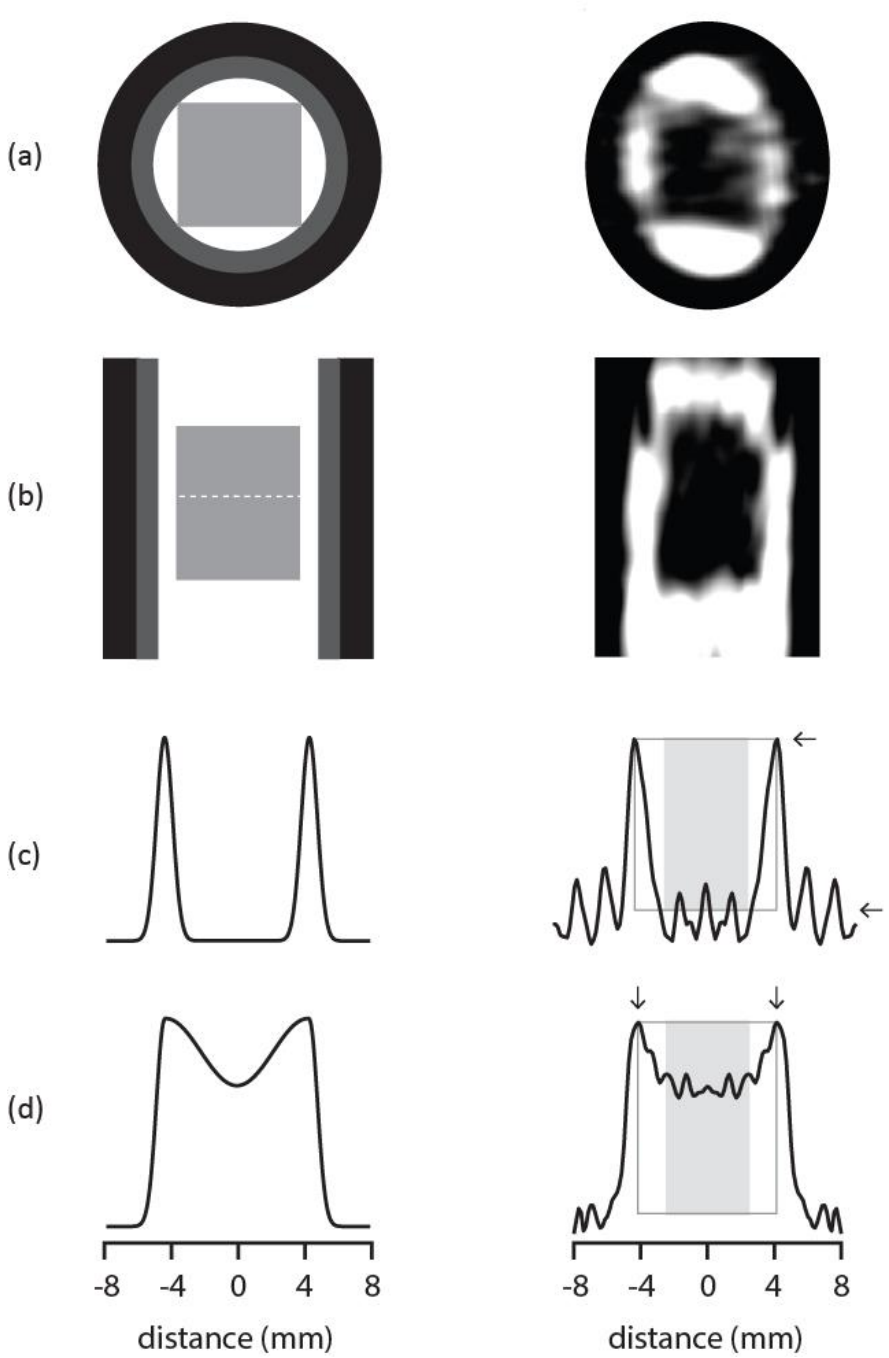

Figure 3.2: The graphics on the left can be used to understand the real MRI data shown on the right. The top and side views of a cubic apple section are described by the gray solid box on the left in (a) and (b). The white region in these 2D diagrams corresponds to the bulk doped solution outside of the cubic apple section. The 1D slices shown in (c) and (d) were obtained at the location of the white dashed line in (b). the open gray box on the right hand side of (c) and (d) indicates the image region where Equation (3.1) is valid while the solid gray box defines the range $0 < \alpha < 1$ in Equation (3.2).

The cubic apple flesh inside of the cylindrical pressure reactor/probe is shown as the light gray square in the top and side views in Figure 3.2(a) and (b) respectively. The dark gray in this image represents the MRI detection coil form and the black denotes the stainless steel pressure reactor. The white space corresponds to the Mn^{2+}-doped water that at short times and at ambient conditions is completely outside of the fruit. A one dimensional (1D) slice through the two dimensional (2D) image at the position of the dashed white line in Figure 3.2(b) yields (c) at short time and (d) at longer time and higher pressure. The right hand column in Figure 3.2 shows real MRI data obtained at 80 MPa applied pressure to cubic apple flesh in Mn^{2+}-doped water. The slices at zero time and midway through the pressurization cycle in (c) and (d) respectively were chosen to reinforce the graphic on the left.

3.4 Theory

It is analysis of the 1D slices like those shown in the right column of Figure 3.2(c) and (d) obtained as a function of time during the pressurization cycles shown in Figure 3.1 that are critical for determining how to efficiently infuse nutrients into the fruit flesh. At short time in Figure 3.2(c) there is no presence of doped water inside of the fruit while at longer times in Figure 3.2(d) the amount of signal in the region of the shaded box increases. At short times the amount of signal in the area indicated by the box is zero, at intermediate times non-zero, and at long times one, if the gray box height (and 1D slice maximum) and width are both normalized to one.

In the experimental limit here, where the amount of doped water inside the fruit at maximum infusion is much less than the doped water inside the entire pressure reactor/probe volume, it is reasonable to assume that the concentration of doped water outside of the fruit remains constant. Moreover, in this study all experiments have shown that the fruit size remains constant throughout the experiment. As an initial, primitive model, consider edge-sourced, one-dimensional bounded diffusion [20]

$$P(x,t) = \sum_{n=0}^{\infty} \cos[2\pi n(\frac{x}{\ell} + \frac{1}{2})] \exp^{-(2\pi n/\ell)^2 D_{inf} t} \tag{3.1}$$

where the distribution P(x,t) corresponds to the concentration of doped water inside the fruit flesh at position x as a function of the time t, ℓ is the side length of the cubic fruit flesh, and D_{inf} is a pressure dependent infusion coefficient. In this way P(x,t) describes the MRI signal from the 1D slices in Figure 3.2(c) and (d) in the region of the open gray box with bounds indicated by the small arrows. The distribution in Equation (3.1) can be used to model the normalized signal obtained by taking the area within the shaded gray box only. In terms of Equation (3.1), this signal is

$$\xi(t) = \frac{\int_{-\alpha\ell/2}^{\alpha\ell/2} P(x,t)dx}{\alpha\ell P(\ell/2,t)} = \frac{1 + \sum_{n=1}^{\infty} (-1)^n \frac{\sin(\alpha n\pi)}{\alpha n\pi} \exp^{-(2\pi n/\ell)^2 D_{inf} t}}{1 + \sum_{n=1}^{\infty} \exp^{-(2\pi n/\ell)^2 D_{inf} t}} \tag{3.2}$$

where $\alpha\ell$ is the horizontal size of the shaded gray box in Figure 3.2(c) and (d). Comparison of the normalized area of the 1D image slices obtained during the pressurization schemes shown in Figure 3.1 to this equation is used to obtain a pressure dependent infusion coefficient D_{inf}. With knowledge of the fruit size ℓ, the saturation time can be defined as $T_{sat} = \ell^2/(2\pi D_{inf})$.

3.5 Materials and Methods

Crystalline manganese chloride tetrahydrate, $MnCl_2 \cdot 4H_20$, from Fisher Scientific and hexane from Sigma Aldrich were both used as received. Gala apples, the fruit used in this study, were obtained from a local grocery store. The hexane was used as the pressure transmission fluid in a syringe pump pressurization system that created hydrostatic pressure inside the pressure reactor/probe. Details regarding the operation of the pressure reactor/probe are provided elsewhere [15].

Cubic, 0.8 cm side length, sections of freshly peeled apple flesh, or apple flesh with peel on one side, were cut and immediately placed into the MRI detection coil inside of the pressure reactor/probe. The pressure reactor/probe was then completely filled with 1 mM Mn^{2+} solution in water, closed, attached the pressure-transfer line filled with hexane and mounted inside of a 0.09 T SMIS imaging electromagnet set to operate at a 4 MHz ^{1}H Larmor frequency and controlled with a Tecmag (Houston, TX) Redstone MRI spectrometer. Each of the four pressurization profiles shown in Figure 3.1, as well as the ambient condition study, involved recording six images, the first at zero time and the remaining five at 35 minute intervals. As pressure reactor/probe pressurization and depressurization took roughly 2 – 5 minutes depending on the size of the pressure differential and the entire assembly was allowed to equilibrate for 5 minutes following any pressure change, a given pressure run took roughly 4.5 hours. All images were obtained with phase encoding and involved 8 signal averages at each point. Longitudinal T_1 and transverse T_2 relaxation times were determined in the usual way from the saturation recovery and Carr-Purcell-Meiboom-Gill pulse sequences [17]. All data manipulation and modeling was accomplished with MATLAB™. Regression of the measured normalized signal area included terms up to n = 200 in Equation (3.2).

3.6 Results and Discussion

The primary goal of this work is to demonstrate that MRI can be used to study in situ high pressure infusion of nutrients into food. The model food system used in this work was peeled apple flesh. Since most interesting nutrients are dissolved in water, the problem simplifies to spatially tracking how bulk water from outside of the fruit is transported into the fruit. By adding paramagnetic Mn^{2+} ions to bulk water, the relaxation times shorten to much less than those for water inside the fruit. At the magnetic field strength used here, the 1 mM Mn^{2+}-doped water yielded T_1 = 145 ms and T_2 = 18 ms while the apple bound water provided $T_1 = T_2$ = 2 s. This fact, along with the relaxation time contrast capability of MRI,

enables discrimination and thus the ability to selectively observe the bulk water slowly penetrating the fruit with added pressure. The real MRI data shown on the right hand side of Figure 3.2 demonstrates that MRI can detect the fruit, as a low intensity square hole, from both the top and side views in (a) and (b) respectively. It is the change in the 1D slice shape as a function of time during pressurization in (c) and (d) that provides information regarding nutrient infusion. Prior to pressurization, in Figure 3.2(c), the bulk Mn^{2+}-doped water is outside of the fruit. Increasing the pressure and waiting leads to the 1D slice in Figure 3.2(d) suggesting that the added pressure enables the bulk, short relaxation time, Mn^{2+}-doped water to penetrate into the apple flesh.

The secondary, but equally important, goal of this work is to use the high pressure MRI experiment to determine which pressurization strategy in Figure 3.1 most efficiently infuses nutrients into food. From the point of view of this experiment, the goal is to discover which pressurization strategy in Figure 3.1 puts the most Mn^{2+}-doped water into the fruit in the shortest amount of time. Four different pressurization strategies and a study at ambient conditions as shown in Figure 3.1(a)-(e), were explored here. The two different runs having high and intermediate applied pressure in Figure 3.1(a) and (c) provide pressure-dependent infusion details. The literature suggests [10] that nutrient infusion is more readily accomplished by either gating the applied pressure or by slowly ramping the pressure from zero to a final value. Comparison of the MRI results obtained with the strategies in Figure 3.1(b) and (c) and between (a) and (d) reveals whether or not pressure gating or ramping improves infusion efficiency. A comparison of the four pressurization strategies in Figure 3.1(a)-(d) to ambient pressure, Figure 3.1(e), reveals how any pressurization strategies compares to infusion with a lack of externally added pressure. As mentioned above, the various pressurization strategies in Figure 3.1 were compared by modelling the area under the 1D image slice as a function of time during the pressurization with Equation (3.2). Other data models could be used, however this one was chosen for basic simplicity. The primary output parameter is an infusion coefficient, D_{inf}, a number that has physical meaning as it is essentially a pressure

driven diffusion coefficient. The results of this modelling effort applied to the pressurization strategies shown in Figure 3.1 are summarized in Table 3-1.

Table 3-1: Effective infusion coefficient, saturation time and length scaling factor obtained from comparing MRI data to Equation (3.2).

pressure cycle†	α	T_{sat} (hrs)	D_{inf} (cm^2/s)
(a)	0.52	1.3	5.99×10^{-5}
(b)	0.52	6.0	1.39×10^{-5}
(c)	0.48	5.6	1.49×10^{-5}
(d)	0.23	8.3	4.87×10^{-6}
(e)	0.19	496.0	1.25×10^{-7}

†see Fig. 1 for pressure cycle.
*R^2 values for fit are in excess of 0.85 on average

Here the scaling factor α relates to the size of the shaded integrated area shown in the right hand column in Figure 3.2(c) and (d). A value of $\alpha = 1$ considers the entire fruit section while $\alpha = 1/2$ limits the area to the center half of the fruit section. The size of D_{inf} reports on how fast the Mn^{2+} doped water enters the fruit and with knowledge of the fruit size T_{sat} or the time it takes to saturate the fruit can be calculated. According to the results in Table 3-1, the higher the pressure, the more efficient the infusion. Any pressurization strategy increases the efficiency of infusion over ambient pressure. There is at least a 50-fold increase in time to saturation, if no external pressure is added. Both D_{inf} and T_{sat} are a factor three more effective for operation at a constant 80 MPa applied pressure in comparison to 20 MPa for the pressure cycles in rows (a) and (c) respectively. Gating the pressure does not seem to further enable mass transport into the fruit as suggested by the slightly larger D_{inf} and concomitantly shorter T_{sat} for a constant versus gated 20 MPa applied pressure in rows (c) and (d) respectively in Table 3-1. Similarly, ramping the

pressure in Figure 3.1(d) also does not encourage mass transport as the D_{inf} and T_{sat} values in row (d) in Table 3-1 are respectively much smaller and larger than for the results for the constant applied 80 MPa pressure in row (a). The data summarized in Table 3-1 strongly suggest that the most efficient way to infuse solutes into peeled sliced fruit with pressure is with as high a constant pressure as possible. There will, of course, be a point where the applied pressure is so high that the fruit shape is physically changed e.g. smashing or crushing. Such physical changes were not observed in any of the studies reported here and it is likely that even operation at the highest pressure available to food processors will also not harm the fruit.

Although the data model in Equation (3.2) is arguably primitive, it does provide a simple and fair way to compare 1D images obtained through a pressure run in terms of a physically meaningful infusion coefficient D_{inf}. The actual values for D_{inf} reported in Table 3-1 also make physical sense as the self - diffusion coefficient $D = 2.3 \times 10^{-5}$ cm^2/s for free water at ambient conditions [21]. For example, Table 3-1 reports that D_{inf} is nearly two orders of magnitude lower at ambient conditions. In other words, without added pressure, very little bulk, Mn^{2+}-doped water enters the fruit. Indeed, D_{inf} for the penetration of water into fruit appears to be less than D in all cases except the highest pressure. At the highest constant pressure studied here, D_{inf} is slightly larger than D suggesting that the applied pressure moves the bulk Mn^{2+} doped water into the apple matrix faster than free molecular diffusion. Higher pressure could be related to faster diffusion; however, it could just be underscoring the fact that D_{inf} is not really a diffusion coefficient but a modelling parameter. Another possibility is that the simple model breaks down at higher pressure. The values for the scaling factor α also make sense given the spatial regions explored in the 1D image slices. Analysis of the 1D images for pressure cycles (a) – (c) involved using half of the fruit section while for pressure cycles (d) and ambient conditions a smaller integration region was used thus α values of 0.5 and 0.2 were found for these respective cases.

The results presented thus far correspond to bulk Mn^{2+}-doped water infusing into cubic, completely peeled, apple flesh. The situation is different when an apple peel is included. The schematics on the left hand side of Figure 3.3 describe what happens in this case as a function of time at pressure.

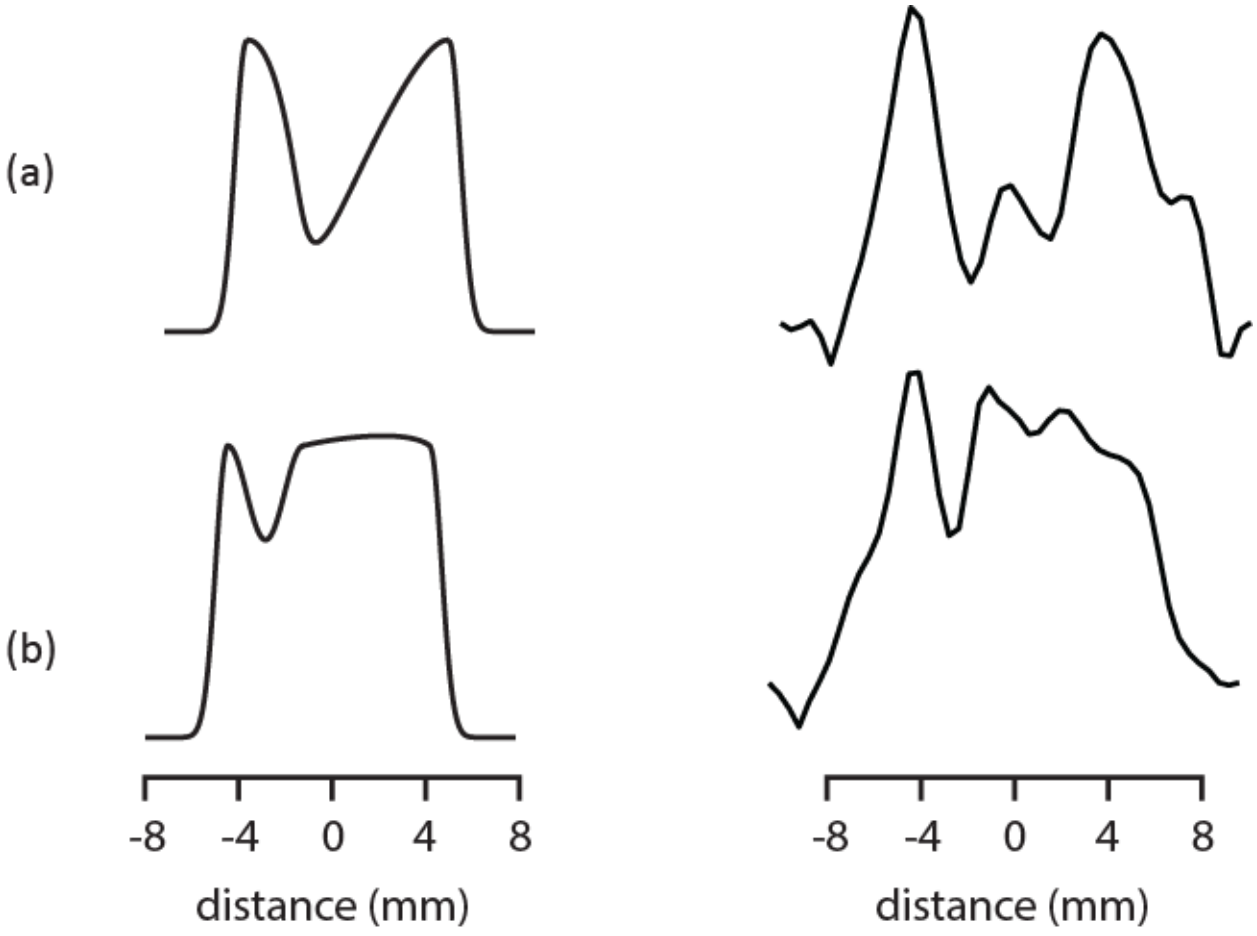

Figure 3.3: The calculated 1D slices on the left can be used to understand the real MRI data on the right obtained at 80 MPa applied external pressure. The peel is located at –4 mm in all images. The 1D image at the short time, or 40 minutes into the pressure run, in (a) appears to fill in from the side opposite the peel in (b) obtained after 160 minutes at pressure.

At very short time the bulk Mn^{2+} doped water is isolated outside of the apple section. At later times, some Mn^{2+}-doped water infuses from all sides except through the peel, thus there is a buildup of signal on the right hand side of the image. The actual MRI data shown on the right hand side of Figure 3.3 are consistent with this prediction, suggesting that the apple peel is less permeable to infusion of the bulk

Mn^{2+}-doped water. This observation is consistent with infusion studies in cranberry where either the skin needed to be removed or disrupted with sandpaper to increase nutrient permeability [2, 10].

The two obvious limitations of this work are the numerical modeling of Mn^{2+} doped water penetration into the fruit captured by Equation (3.2) and the idea that nutrients and bulk water similarly pass into fruit with added pressure. As mentioned above, the numerical model of edge-sourced bounded 1D diffusion was chosen for its simplicity and the similarity of the distributions calculated from Equation (3.1) and the measured data like those shown in the right column in Figure 3.2(c) and (d). The model clearly neglects nutrient filling the fruit from directions perpendicular to the 1D MRI slice direction. Accounting for this fact in addition to numerically solving the diffusion equation with proper boundary conditions would clearly help in properly understanding the evolution of the 1D images as a function of time. However, since the end product will still be an infusion coefficient that can be used to decide which pressurization strategy in Figure 3.1 is most efficient, this was not pursued here. The relevance of this work relies on the idea that real nutrients will pass into the fruit with the bulk water and that by tracking how the bulk water infuses into the fruit matrix, the location of the nutrients is inferred. To track the bulk water, paramagnetic Mn^{2+} cations are added to enhance nuclear spin relaxation. These ions, like nutrients, are transported into the fruit flesh with the bulk water at pressure. It is likely that larger nutrients, like soluble proteins, will not permeate the fruit flesh in the same way as the smaller Mn^{2+} cations and water. This can, in principle, be explored by repeating this work with a larger, water stable, non – reactive paramagnetic macromolecule or an electron spin labeled nutrient that replaces the Mn^{2+} cation. Comparison of the 1D images at constant pressure and time as a function of paramagnetic solute size would answer this question and is the subject of future work.

3.7 Conclusion

This work demonstrates that MRI combined with an off-the-shelf pressure reactor customized with an MRI detection circuit [15] can be used to study the high-pressure infusion of nutrients into food. It was also determined that any pressure strategy outperforms ambient-pressure infusion, but that neither pressure gating nor ramping offered any obvious advantage among the high-pressure strategies for nutrient infusion performance. Moreover, operation at the highest pressure possible should provide the best infusion performance as long as the fruit is not physically changed or crushed. The MRI results for unpeeled fruit suggests, consistent with the literature [10, 11], that the peel significantly attenuates the infusion of bulk Mn^{2+} doped water into the apple section. Future work will consider the effect of peel treatment on mass transport. With this MRI approach, entire small fruits, like blueberries or cranberries, can be placed into the pressure reactor/probe and Mn^{2+}-doped water penetration could be tracked as a function of peel treatment, roughness, or perforation.

3.8 References

[1] Karwe, M.; Salvi, D.; Gosavi, N.S. High pressure-assisted infusion in foods. *Ref. Modul. Food Sci.* **2016**.

[2] Mahadevan, S.; Salvi, D.; Karwe, M.V. High pressure-enhanced infusion in fresh and frozen-thawed cranberries: a comparative study. *J. Food Process Eng.* **2015**, *39*, 53-60.

[3] Bawa, A.S.; Anilakumar, K.R. Genetically modified foods: safety, risks and public concerns—a review. *J Food Sci Technol.* **2013,** *50*, 1035–1046.

[4] Goicoechea, N.; Antolín, M. C. Increased nutritional value in food crops. *Microb. Biotechnol.* **2017**, *10,* 1004-1007.

[5] Trivedi, P.; Schenk, P.M.; Wallenstein, M.D.; Singh, B.K. Tiny microbes, big yields: enhancing food crop production with biological solutions. *Microb. Biotechnol.* **2017**, *10*, 99-1003.

[6] Fito, P.; Chiralt, A.; Barat, J. M.; Spiess, W.E.L.; Behsnilian, D. Osmotic Dehydration and Vacuum Impregnation: Applications in Food Industries. **2001.** *Technomic,* New York.

[7] Dewettinck, K.; Van Bockstaele, F.; Kühne, B.; Van de Walle, D.; Courtens, T.M.; Gellynck, X. Nutritional value of bread: Influence of processing, food interaction and consumer perception, *J Cereal Sci.* **2008,** *48*, 243-257.

[8] Teferra, T.F. Should we still worry about the safety of GMO foods? why and why not? A review. *Food Sci Nutr.* **2021**, *9*, 5324-5331.

[9] Gosavi, N.S.; Salvi, D.; Karwe, M.V. High pressure-assisted infusion of calcium into baby carrots part I: influence of process variables on calcium infusion and hardness of the baby carrots. *Food Bioproc Tech.* **2019**, *12*, 255-266.

[10] S. Mahadevan, N. Nitin, D. Salvi, M.V. Karwe, High-pressure enhanced infusion: influence of process parameters. *J. Food Process Eng.* **2015**, *38***,** 601–612

[11] George, J.M.; Selvan, T.S.; Rastogi, N.K. High-pressure-assisted infusion of bioactive compounds in apple slices. *Innov. Food Sci. Emerg. Technol.* **2016**, *33*, 100-107.

[12] Gosavi, N.S.; Salvi, D.; Karwe, M.V. High pressure-assisted infusion of calcium into baby carrots part II: influence of process variables on beta-carotene extraction and color of the baby carrots. *Food Bioproc Tech.* **2019**, *12*, 613-624.

[13] Muntean, M.; Marian, O.; Barbieru, V.; Cătunescu, G.M.; Ranta, O.; Drocas, I.; Terhes, S. High pressure processing in food industry – characteristics and applications. *Agric. Agric. Sci. Procedia.* **2016**, *10*, 377-383.

[14] Balasubramaniam, V.M.; Farkas, D. High-pressure food processing. *Food Sci. Technol Int.* **2008**, *14*, 413-418.

[15] Kerr, J.D.; Balcom, B.J.; Augustine, M.P. A low cost, portable NMR probe for high pressure, MR relaxometry. *J. Magn. Reason.* **2019**, *304*, 35–41.

[16] Mamin, H.; Poggio, M.; Degen, C. Nuclear magnetic resonance imaging with 90-nm resolution. *Nature Nanotech.* **2007**, *2*, 301–306.

[17] Harris, R. Nuclear Magnetic Resonance Spectroscopy. **1986.** Longman, Harlow.

[18] Vlaardingerbroek, M.T.; Boer, J.A. Magnetic Resonance Imaging: Theory and Practice. **2003.** Springer-Verlag Berlin Heidelberg, New York.

[19] Young, S.W. Nuclear Magnetic Resonance Imaging: Basic Principles. **1984.** Raven Press.

[20] Crank, J. The Mathematics of Diffusion. **1956**. Clarendon Press, Oxford.

[21] Krynicki, K.; Green, C.D.; Sawyer, D.W. Pressure and temperature dependence of self -diffusion in water. Faraday Discuss. Chem. Soc. **1978**, 66, 199-208.

Chapter 4. A variable pressure, NMR relaxometry study of sodium silicate

4.1 Abstract

There is a continual need for nuclear magnetic resonance (NMR) instrumentation that is amenable to ill-defined and messy samples. A high volume high pressure probe, made from commercially available parts was recently developed and used to accomplish this study [1]. In order to more fully demonstrate the utility of the pressure reactor probe assembly a multinuclear ^{23}Na and ^{1}H study of sodium silicate, Na_2SiO_3, was accomplished at pressures up to 100 MPa. Two magnets were used in this work. A small portable opposing pole-facing permanent magnet was used to study ^{23}Na while a much larger format small body imaging permanent magnet was used to explore ^{1}H. Both relaxation and diffusion coefficient measurements as a function of pressure were accomplished. Results suggest that Na_2SiO_3 is a non-Newtonian fluid and does not exist within the extreme narrowing limit. These results are consistent with the observed adhesive properties of Na_2SiO_3.

4.2 Introduction

Although sample characterization by NMR spectroscopy is well known at ambient conditions, special hardware is still needed to accomplish measurements at elevated pressure [2]. High pressure NMR is no longer limited by commonly available small probe volumes and delicate, expensive hardware. A high pressure, high volume NMR probe was developed a few years ago that lends itself to messy, ill-defined, and difficult to study samples [1]. Samples that have previously been barred from high pressure NMR study are now available for characterization. This NMR probe has already been described in detail and been used in food-related magnetic resonance imaging (MRI) studies [1, 3]. This probe continues to be

tested and used to demonstrate the array of difficult samples that are now accessible to high pressure NMR. This more challenging work reports a multinuclear study on an adhesive, sodium silicate Na_2SiO_3, that rapidly dries and hardens. Data were collected via the use of this high pressure probe. The complicated rheology of the adhesive and the difficulty of dealing with a heteronuclear sample were easily overcome with this pressure reactor probe.

Silicates are of interest to many ranges of chemists, geochemists, and engineers [4]. The application and study of silicates are seemingly endless. Sodium silicate is not an exception. The uses for Na_2SiO_3 are vast, including adhesives [5], detergents [6], and construction materials [7]. Sodium silicate is also used in wastewater treatment [8], as well as an additive in many cosmetics and certain skin care products [9].

Other high-pressure NMR instruments are not amenable to adhesive sodium silicate, which could damage some instruments. Sodium silicate poses a problem for traditional, expensive high-pressure NMR assemblies. For example, the 3.0 mm ID of the zirconia tube pressure cell produced by Daedalus Innovations is far too narrow to allow proper cleaning after an adhesive sample [10]. This messy material requires thorough mechanical cleaning between samples that would ruin the precious zirconia cell. Adhesives are even more destructive in NMR pressure probes like the ones developed by Jonas [11] and Casey [12]. Possibilities of having the moving parts of those pressure cells glued shut due to a sample leak would be ruinous. A robust pressure reactor probe assembly is the solution to samples like this that were previously inaccessible through high-pressure NMR.

Previous work demonstrated that this high-pressure probe can accomplish NMR relaxometry on ^1H nuclei at room temperature and elevated pressure [1]. In addition, the same probe was used to accomplish ^1H MRI on food samples to study high-pressure nutrient infusion [3]. Heteronuclear studies up until this point have yet to have been attempted. In this study, the system interfaces with two more

magnet assemblies. The work reported here describes how to extend the usefulness of this NMR probe assembly for ^{23}Na heteronuclear NMR and ^{1}H NMR pulsed-field-gradient-based diffusion coefficient measurements.

4.3 Material and Methods

The 42 % sodium silicate solution in water used in this study, and referenced here as Na_2SiO_3, was used as received from Millipore. Hexane was used as received from Sigma – Aldrich.

Inversion recovery, spin echo, Carr-Purcell-Meiboom-Gill (CPMG), and pulsed-gradient spin-echo (PGSE) pulse sequences were all used in this study to characterize Na_2SiO_3 at elevated pressure. Acquisition of associated signals was accomplished using Tecmag Redstone NMR spectrometers. A high volume, high pressure NMR probe developed in house was used to both deliver pressure and collect the requisite NMR signal [1]. The Na_2SiO_3 system relaxation times were measured at ambient pressure (0.1 MPa), 50MPa, and 100MPa. The hydrostatic pressure used in these experiments was delivered by a syringe pump. Hexane was used as the pressure transmission fluid.

Two magnet assemblies were used in this study. All ^{23}Na NMR data were obtained from a SpinCore, Inc. 440 mT, permanent opposing pole-facing magnet with a 3 cm access gap. All ^{1}H NMR data were obtained from an Aspect M2 1 T permanent imaging magnet, with a 6.3 cm high x 10.8 cm wide bore. The timing diagrams shown in Figure 4.1 (a) and (b) correspond to the inversion recovery and spin echo pulse sequences for ^{23}Na. These pulse sequences were used to measure the ^{23}Na T_1 and T_2^{echo} relaxation times in Na_2SiO_3 as a function of pressure using the SpinCore magnet. In both of these experiments, 6,000 acquisitions for each t_1 point were averaged, 50 t_1 points were obtained with an indirect dwell time of dt_1 = 100 μs and 1,024 points were directly measured with a direct dwell time of dt_2 = 25 μs. Inversion recovery, CPMG, and PGSE pulse sequences, shown in Figure 4.1 (a), (c), and (d),

were used to measure the ^{1}H T_1, ^{1}H T_2^{cpmg}, and ^{1}H diffusion coefficient (D) values. ^{1}H T_1, ^{1}H T_2^{cpmg}, and ^{1}H diffusion values at various pressures were obtained using the Aspect M2 magnet.

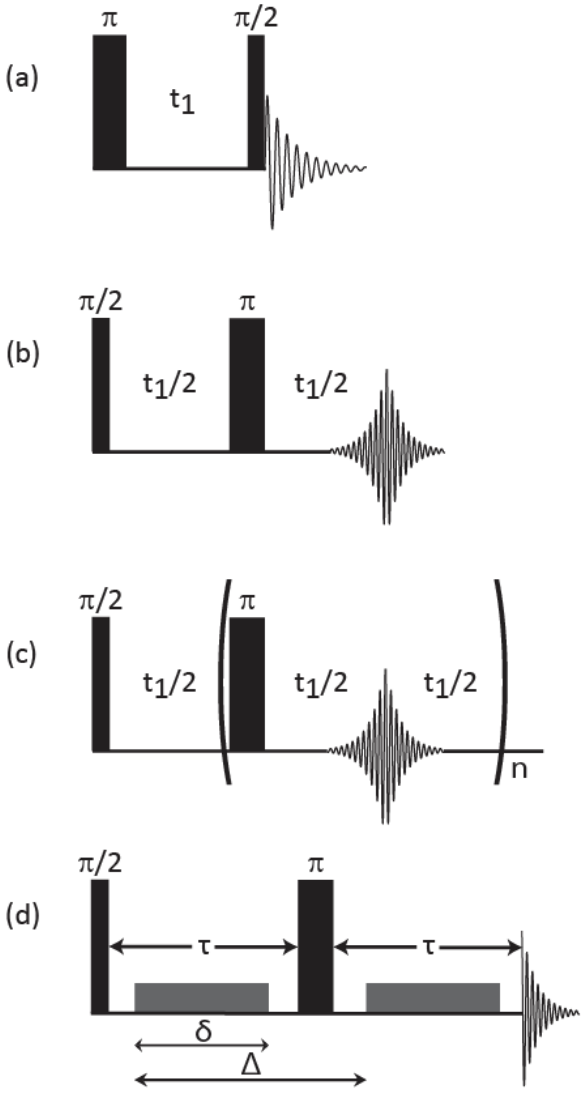

Figure 4.1: Timing diagrams for the NMR pulse sequences used in this work. The inversion recovery pulse sequence in (a) and the spin echo pulse sequence in (b) were used to measure ^{23}Na T_1 and T_2^{echo} values as a function of pressure, while (a) and the pulse sequence in (c) were used to measure ^{1}H T_1 and T_2^{cpmg} values. The PGSE sequence in (d) was used to determine D values.

4.4 T_1 and T_2^{echo} ^{23}Na Relaxation of Na_2SiO_3

A summary of the ^{23}Na T_1 and T_2^{echo} values as a function of pressure is shown in Figure 4.2.

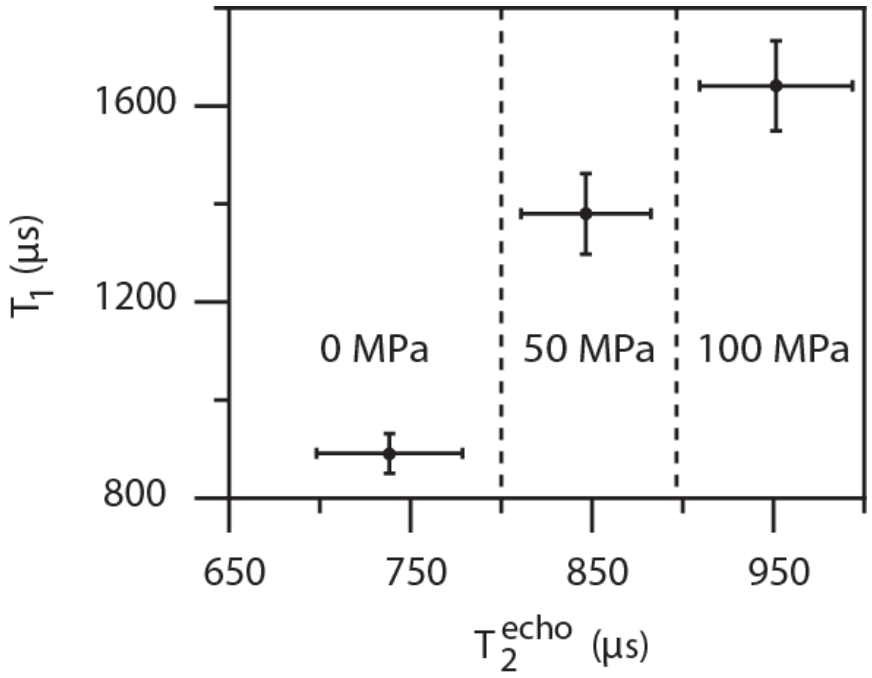

Figure 4.2: Summary of the ^{23}Na T_1 and T_2^{echo} values for Na_2SiO_3 as a function of pressure.

The values are measured from separate pulse sequences and are not true relaxometry correlations. Pressure increases from left – to – right in Figure 4.2. The increase in ^{23}Na T_1 implies that added pressure increases the viscosity of Na_2SiO_3 which reduces the effective sample mobility, which in turn increases the ^{23}Na T_2^{echo} value. It is clear from Figure 4.2 that $T_1 >> T_2^{echo}$ for ^{23}Na. Indeed, the ^{23}Na T_2^{echo} was so short that the CPMG sequence yielded the same value. This difference implies that the sample is not in the extreme-narrowing limit, which forces $T_1 \neq T_2^{echo}$ or T_2^{cpmg} and makes $T_1 \approx \tau_c$ or that as pressure increases, viscosity increases, τ_c increases, and the ^{23}Na T_1 value becomes larger.

4.5 T_1, T_2^{cpmg} ^{1}H Relaxation of Na_2SiO_3

A summary of ^{1}H T_1 and T_2^{cpmg} values as a function of pressure is shown in Figure 4.3. Again, the values here are measured from separate pulse sequences and are not true correlations.

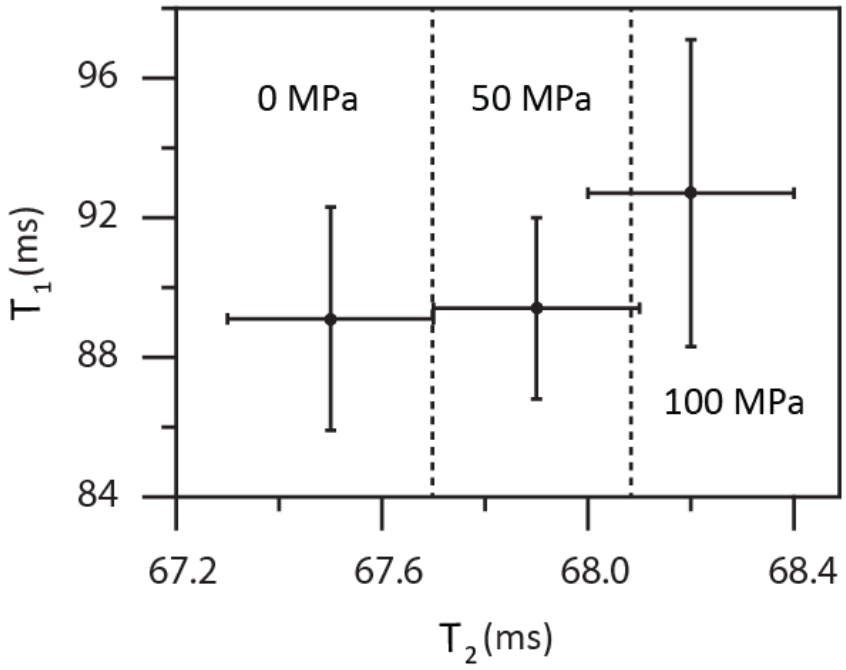

Figure 4.3: Summary of the ^{1}H T_1 and T_2^{cpmg} values for Na_2SiO_3 as a function of pressure.

Pressure again increases from left – to – right in Figure 4.3. Inversion recovery and CPMG pulse sequences were used to measure the ^{1}H T_1 and T_2^{cpmg} values for Na_2SiO_3 as a function of pressure using the Aspect M2 imaging magnet.

Unlike the case for ^{23}Na, the ^{1}H relaxation time values are largely unchanged with respect to pressure. This result is unsurprising as the two nuclei relax to thermal equilibrium via two different mechanisms. For the I = 1/2, ^{1}H nuclear relaxation is controlled by time-dependent fluctuations in the ^{1}H – ^{1}H dipolar coupling. The time constant that characterizes the time scale of the fluctuations that

incoherently modulate this dipolar coupling is τ_c. In the case of I = 3/2, ^{23}Na relaxation is controlled by the quadrupolar coupling of the nuclear spin to the electric-field gradient at the site of the nucleus. In this case it is not relative nuclear spin motion that governs the relaxation rate, rather it is the incoherent time-dependent modulation of the electric-field gradient at the ^{23}Na nucleus by sudden changes to the sodium coordination sphere. Again, the time constant for this motion is τ_c. Perhaps the more intrinsic aspect is that again $T_1 >> T_2^{cpmg}$ and that the sample is not in the extreme-narrowing limit. Although ^{1}H relaxometry does not in itself provide pressure dependent relaxation, as the relaxation mechanisms are different between ^{23}Na and ^{1}H nuclei, it does provide a useful metric. It appears that Na_2SiO_3 has intrinsic mobility properties that remove it from the extreme narrowing limit.

4.6 ^{1}H Diffusion Measurements

The ^{1}H based PGSE pulse sequence was used to explore the viscosity of the fluid. In the special case of a Newtonian fluid, the Stokes-Einstein equation can be used to relate the diffusion coefficient to viscosity. The largely pressure independent results shown in Fig. 4 suggest that pressure does not affect the diffusion coefficient and thus, viscosity of Na_2SiO_3, in contrast to the ^{23}Na NMR results.

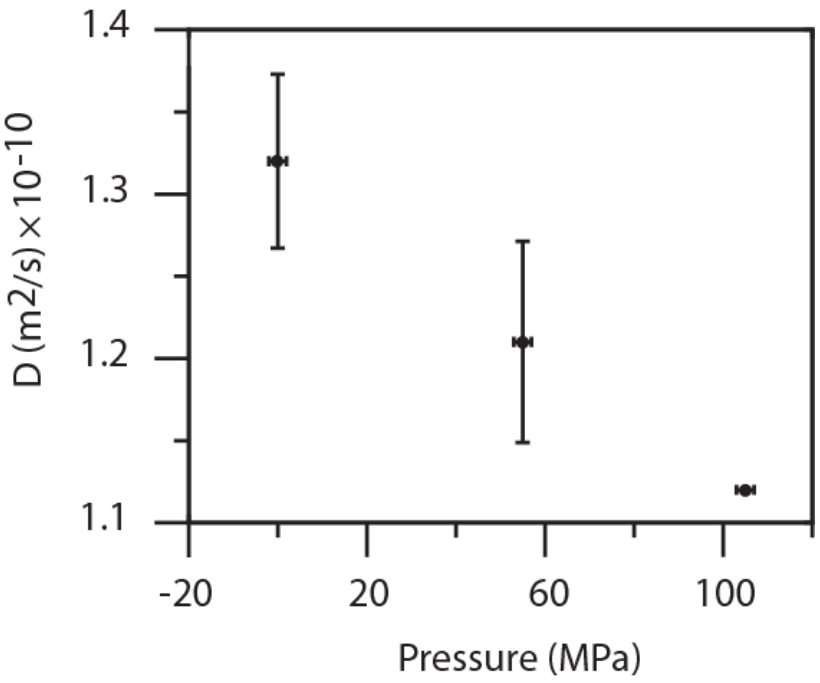

Figure 4.4: Summary of the ^{1}H NMR determined D values as a function of pressure.

This discrepancy is likely due to the fact Na_2SiO_3 is not a Newtonian fluid at elevated pressure, as suggested by the departure from the extreme-narrowing limit in both the ^{23}Na and ^{1}H relaxometry results in Figs. 2 and 3, and thus the diffusion coefficient is not easily and straight forwardly related to viscosity. In order to retrieve the true viscosity with NMR methods one would have to resort to controlled measurements at elevated pressure on flowing or moving samples, a measurement for which no hardware is currently available.

4.7 Conclusion

A multinuclear study, including ^{23}Na and ^{1}H, of an aqueous solution of adhesive, sodium silicate, was performed at elevated pressure. A new design for a high pressure NMR probe amenable to difficult and ill-defined samples was leveraged. Inversion recovery, CPMG, spin echo, and PGSE pulse sequences were used on either ^{23}Na or ^{1}H nuclei to measure T_1, T_2^{echo}, T_2^{cpmg} and D. Measurements were obtained

from ^{23}Na and ^{1}H nuclei using two different magnets, an opposing pole-facing magnet from SpinCore, Inc. and a small-body imaging magnet from Aspect. The NMR relaxometry data for both nuclei suggest that the extreme-narrowing limit does not apply to Na_2SiO_3 and that it should be expected that the diffusion coefficient is not simply related to the sample viscosity. Indeed, ^{1}H diffusion measurements obtained from the imaging magnet did not display any pressure dependence, suggesting either it is a non-Newtonian liquid, or that the ^{23}Na relaxometry is not related to bulk, macroscopic translational motion but instead relates to local microscopic fluctuations of the electric-field gradient around the ^{23}Na nucleus. In closing, it is important to note that these measurements would not be possible using commonly available NMR hardware due to the harmful nature of the sample.

4.8 References

[1] J. D. Kerr, B. J. Balcom and M. P. Augustine, "A low cost, portable NMR probe for high pressure, MR relaxometry," *J. Magn. Reson.,* vol. 304, pp. 35-41, 2019.

[2] R. W. Peterson and A. J. Wand, "Self-contained high-pressure cell, apparatus, and procedure for the preparation of encapsulated proteins dissolved in low viscosity fluids for nuclear magnetic resonance spectroscopy," *Rev. Sci. Instrum.,* vol. 76, 2005.

[3] J. D. Kerr, D. M. Gruber and M. P. Augustine, "Using MRI to study high pressure assisted nutrient infusion," *In preparation..*

[4] H. Koller, G. Engelhardt and J. Felsche, "Variable temperature ^{1}H, ^{23}Na, and ^{29}Si MAS NMR studies on sodium silicate hydrates of composition Na_2O SiO_2 nH_2O (n = 9, 6, 5): local structure in crystals, melts, supercooled melts, and glasses," *Z. anorg. allg. Chem.,* vol. 621, pp. 301-310, 1995.

[5] H. Y. Wang, R. S. Foote, S. C. Jacobson, J. H. Schneibel and J. M. Ramsey, "Low temperature bonding for microfabrication of chemical analysis devices," *Sens. Actuators B: Chem.,* vol. 45, no. 3, pp. 199-207, 1996.

[6] G. Lagaly, W. Turfar, A. Minihan and A. Lovell, "Silicates," in *Ullmann's Encyclopedia of Industrial Chemistry*, Weinheim, Wiley-VCH Verlag GmbH & Co. KGaA, 2000, pp. 509-572.

[7] J. L. Thompson, M. R. Silsbee, P. M. Gill and B. E. Scheetz, "Characterization of silicate sealers on concrete," *Cem. Concr. Res.,* vol. 27, no. 10, pp. 1561-1567, 1997.

[8] R. K. Iler, The Chemistry of Silica, Wiley, 1979.

[9] "Final report on safety assessment of potassium silicate, sodium metasilicate, and sodium silicate," *Int. J. Toxicol.,* vol. 24, pp. 103-117, 2005.

[10] "Daedelus Innovations," [Online]. Available: https://daedalusinnovations.com/.

[11] J. Jonas, "Nuclear magnetic resonance measurements at high pressure," *Rev. Sci. Instrum. ,* vol. 43, pp. 643-649, 1972.

[12] B. G. Pautler, C. A. Colla, R. L. Johnson, P. Klavins, S. J. Harley, C. A. Ohlin, D. A. Sverjensky, J. W. Walton and W. H. Casey, "A high-pressure NMR probe for aqueous geochemistry," *Angew. Chem.,* vol. 126, pp. 9946-9949, 2014.